International Journal of Mining Science and Technology 35 (2025) 1731–1751

Contents lists available at ScienceDirect

International Journal of Mining Science and Technology

journal homepage: www.elsevier.com/locate/ijmst

Study on mechanical properties and mesoscopic damage mechanism of composite jointed rock masses

Yao Bai [a], Zhibo Xu [a], Haoyu Dou [b,*], Nianzeng Liu [a], Ziyue Zhao [a], Sihao Qiu [a], Renliang Shan [a]

[a] *School of Mechanics and Civil Engineering, China University of Mining and Technology-Beijing, Beijing 100083, China*
[b] *China Nonferrous Metal Mining (Group) Co., Ltd., Beijing 100029, China*

A R T I C L E I N F O

Article history:
Received 16 June 2025
Received in revised form 3 August 2025
Accepted 27 August 2025
Available online 25 October 2025

Keywords:
Composite jointed rock mass
Joint roughness coefficient (JRC)
Failure mode
Energy evolution
Damage parameter

A B S T R A C T

Joints are widely distributed structural defects in rock masses, and their geometric characteristics play a decisive role in the overall stability of rocks under complex stress conditions. To clarify the influence of joint geometry on the mechanical behavior of jointed rock under such conditions, this study investigated the mechanical properties and failure mechanisms of composite jointed rock specimens with varying joint roughness and joint dip angles. Three typical failure modes under triaxial loading were identified, and a mechanical analysis model incorporating joint roughness and dip angle was established. The failure mechanism was revealed, and a discrete element model was developed to analyze the micro-damage evolution process of the specimens. The results show that the mechanical parameters of the specimens exhibit pronounced anisotropy. Both the elastic modulus and peak strength reach their minimum values at a joint dip angle of 60°. Increasing joint roughness significantly reduces the degree of anisotropy and enhances the energy storage capacity of the specimens. A strong linear relationship is observed between the elastic strain energy and the peak deviatoric stress, confirming the applicability of the linear energy storage law in composite jointed rocks. Discrete element simulations revealed the evolution path and dominant types of microcracks between the joint and matrix. The joint dip angle governs the transition of dominant crack types from tensile to shear and then back to tensile. Increased joint roughness significantly suppresses damage localization along the joint and results in an approximately 20% increase in the proportion of shear microcracks within the matrix. These findings clarify the regulatory role of joint geometrical parameters in the damage evolution process.

1. Introduction

In geotechnical and mining engineering, the stability and bearing capacity of rock masses are key factors in design and construction. Joints, as a common type of defect, are widely distributed within rock masses [1], significantly altering their mechanical properties [2,3] and increasing the likelihood of instability and failure. Composite jointed rock masses are commonly encountered in complex geotechnical engineering scenarios such as deep roadways, cross-lithological tunnels, high and steep slopes, and underground mines, as shown in Fig. 1. During deep excavation, such rock masses are typically subjected to a three-dimensional stress field comprising self-weight stress, horizontal tectonic stress, and mining-induced additional stress [4–6]. Their failure modes are significantly influenced by joint dip angle and joint roughness [7]. Specifically, during loading, rough joint surfaces generate shear friction, which promotes crack initiation at the joint tips; these cracks propagate and coalesce, eventually forming shear bands. Numerous engineering practices have shown that composite jointed rock masses are prone to localized large deformations during construction, potentially leading to global instability of the rock mass and greatly increasing construction risk [8–10]. Therefore, understanding the failure mechanisms of composite jointed rock masses under triaxial conditions remains a key challenge in related research fields.

In recent years, many researchers have conducted mechanical tests and analyses on jointed rock masses, yielding substantial results. Liu et al. [11] performed uniaxial compression tests on granite specimens with Y-shaped joints to investigate the effects of intersecting rough joints on strength, failure modes, and precursor damage characteristics. The results revealed that the joint dip angle and joint roughness significantly influence the uniaxial compressive strength and that different failure modes emerge at various thresholds. Asadizadeh et al. [12] employed 3D printing technology to fabricate artificial specimens with non-persistent

---

* Corresponding author.
E-mail address: dhy97001@163.com (H. Dou).

https://doi.org/10.1016/j.ijmst.2025.08.018
2095-2686/© 2025 China University of Mining & Technology. Publishing services by Elsevier B.V.

(a) Composite joint surrounding rock

(b) Local deformation of the composite joint surrounding rock

Fig. 1. Jointed surrounding rock in the roadway.

rough joints and carried out uniaxial compression tests. Through multivariate statistical analysis, they explored the influence of four parameters—joint roughness coefficient (JRC), bridge length, bridge angle, and joint dip angle—on the uniaxial compressive strength, deformation modulus, and crack initiation stress, and further classified the failure modes into six categories on the basis of crack propagation. Huang et al. [13] found that in low-permeability rocks in cold regions, frost-induced stress around elliptical cavities is concentrated at the ends of the major axis, easily initiating fractures in that direction. Freeze-thaw cycles accelerate crack propagation, forming a network of fractures. Yan et al. [14] conducted discrete element simulations on granite with flaws to study crack evolution and failure mechanisms, revealing that flaws serve as stress concentrators that trigger crack propagation. Yuan et al. [15] prepared sawtooth joint specimens using 3D printing and cement mortar, and performed uniaxial compression tests. The results indicated that joint roughness and inclination significantly influence the strength and deformation characteristics of jointed rock masses, inducing transitions in the failure mode from tensile splitting or shear sliding to tensile-shear mixed failure. Peellage et al. [16] conducted cyclic triaxial tests on jointed rock masses and reported that joints significantly affect the dynamic response under cyclic loading. Joint slip and microcrack propagation increased the hysteresis loop area and energy dissipation. When the amplitude exceeded a critical value, the jointed rock masses exhibited three-stage damage evolution characterized by "elastic–plastic-failure" behavior. Chen et al. [17] performed triaxial tests on specimens that had undergone direct shear tests to investigate the mechanical behavior and strength characteristics of non-penetrating jointed rocks. The results showed that under high normal stress, the specimens exhibited low cohesion but high internal friction angles.

The above research is mainly concentrated on the mechanical characteristics and failure patterns of rock masses containing different defects. However, little attention has been given to jointed rocks with different matrix strengths across joints. Previous studies have demonstrated that variations in matrix strength across joints significantly affect the mechanical parameters of jointed rocks [18,19]. Many scholars have carried out mechanical tests on composite rocks [20,21], revealing that the strength of such composites typically lies between the strengths of strong and weak matrices. Furthermore, the deformation process is governed mainly by the weaker matrix. However, most of the current research on composite jointed rock masses focuses on coal-rock combinations. The weak side matrix of such research objects often has an excessively low strength. In actual engineering, the weak side matrix is not limited to coal, which is a low-strength rock mass. Moreover, in these research works, the influence of joint parameters is often ignored. It is of great significance to conduct research on the mechanical properties of composite jointed rock masses with different joint roughness and joint dip angles.

On this basis, composite jointed specimens with varying joint roughness and joint dip angle were prepared. A systematic investigation was conducted using a combination of laboratory experiments, numerical simulations, and theoretical analyses to elucidate the influence of joint geometry and asymmetric matrix strength on the mechanical properties and failure mechanisms of the specimens. Through detailed analysis of the experimental results, including stress-strain behavior and energy evolution characteristics, together with meso-scale damage evolution and the development of mechanical models, the deformation and failure patterns of composite jointed rock masses under loading were comprehensively revealed. This study aims to provide a robust theoretical framework and experimental evidence to advance the understanding of the mechanical behavior of structurally complex rock masses.

2. Experimental preparation

2.1. Selection of rock-like materials

Due to the inherent randomness and uncontrollability of natural jointed rock masses, experimental results often exhibit significant scatter. This makes it difficult to isolate the effects of specific variables and eliminate interference from non-target factors [22–25]. To address this issue, the present study adopts similar material modeling for laboratory testing. Based on previous studies [26–28], composite jointed rock specimens with material heterogeneity on either side of the joint were prepared by adjusting the mix proportions of the cement mortar. Material A was designed with a higher cement content to exhibit greater compressive strength and stiffness, simulating the strong lithologies commonly encountered in coal mines, such as limestone and hard sandstone within roof strata. In contrast, material B contained a greater proportion of sand, resulting in a lower strength and stiffness, representing weak surrounding rock, such as sandy mudstone, is frequently observed in the soft roof or floor conditions of roadways. Field observations indicate that the uniaxial compressive strength (UCS) ratio between medium-hard sandstone and mudstone typically ranges from 1.5:1 to 3:1 in coal-bearing strata [29]. Accordingly, a UCS strength ratio of 2:1 was adopted to represent the mechanical contrast between the two lithologies.

In this study, two types of rock-like materials were prepared using P42.5 cement, standard sand, and water with mass ratios of 1:1:0.25 (Material A, gray cement) and 1:1.5:0.45 (Material B, white cement). The comparison of uniaxial compression stress-strain curves between two types of rock materials and the original rocks are shown in Fig. 2.

The basic mechanical properties of the two materials, derived from the above experiments, are summarized in Table 1. The adopted mix proportions are suitable for modeling a composite jointed rock mass with asymmetric matrix strengths.

2.2. Preparation of composite jointed rock mass specimens

Due to various limitations associated with natural joints under laboratory conditions, meeting the precision and repeatability requirements of this study is difficult. Therefore, regular sawtooth joints are used in place of natural joints [30]. Using 3D printing technology, joint molds were fabricated and combined with similar materials to produce composite jointed rock mass specimens. The prepared specimens are shown in Fig. 3.

In this study, the JRC of the joint surface is calculated based on the fractal dimension theory proposed by Xie [31].

$$D = \lg 4 / \lg\{2[1 + \cos(\arctan(2H/L))]\} \tag{1}$$

$$\mathrm{JRC} = 85.267(D - 1)^{0.5679} \tag{2}$$

where D represents the fractal dimension; L the average base length; and H the height of the undulation angle.

Based on the above equations, the average base length for determining the JRC is set to 5 mm, and the JRC values are selected as 5, 10, and 15. The specific geometric parameters are shown in Table 2.

A Zortrax M200 3D printer was subsequently used to fabricate structural surface molds with varying inclinations and specified roughness (Fig. 4). The ABS resin polymer was selected as the printing material because of its excellent chemical resistance and wear resistance [32,33], which effectively prevents corrosion and abrasion of the joint surfaces. The semi-jointed specimens prepared in this study are illustrated in Fig. 5, and the fabrication process of the composite jointed rock mass specimens is illustrated in Fig. 6.

Table 1
Mix proportions and mechanical parameters of rock-like materials.

Material number	Material A	Material B
Ratio (cement:sand:water)	1:1:0.25	1:1.5:0.45
Uniaxial compressive strength (MPa)	82	41
Tensile strength (MPa)	7.9	4.1
Elastic modulus (GPa)	9.0	4.2
Poisson's ratio	0.2	0.3
Cohesion (MPa)	22.7	14.4
Internal friction angle (°)	30.6	18.0

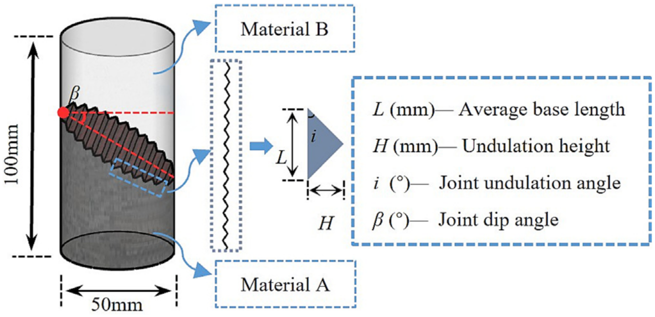

Fig. 3. Schematic illustration of the composite jointed rock mass specimen.

2.3. Testing instruments and experimental scheme

To investigate the influence of joint dip angle (β) and JRC on the mechanical properties of composite jointed rock masses, the confining pressure (σ_3) was set at a constant value (8 MPa). The JRC was set as 5, 10, and 15, while the joint dip angles were designed as five different values: 0°, 30°, 45°, 60°, and 90°. The experimental design scheme is shown in Table 3. To ensure the stability of the experimental results, a minimum of five specimens were prepared

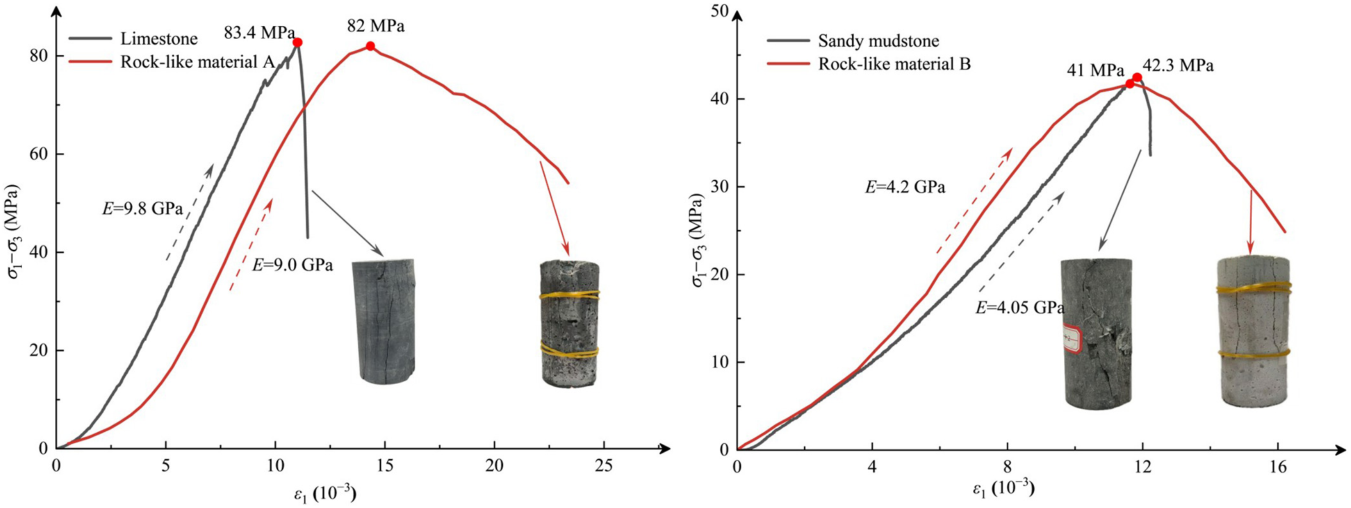

(a) Material A and limestone

(b) Material B and sandy mudstone

Fig. 2. Comparison of stress-strain curves between two kinds of rock-like materials and the original rocks.

Table 2
Geometric parameters of the sawtooth joints.

JRC	Joint geometry
5	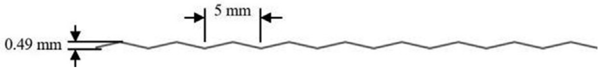
10	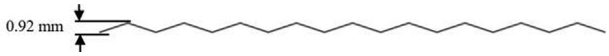
15	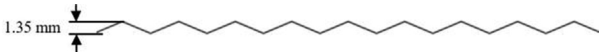

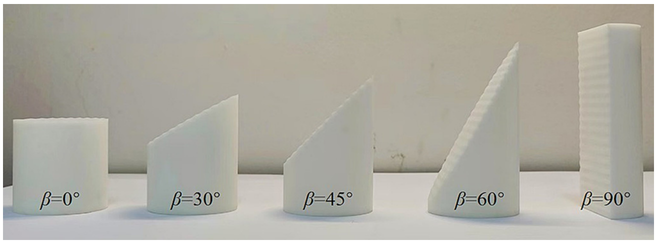

Fig. 4. Joint molds.

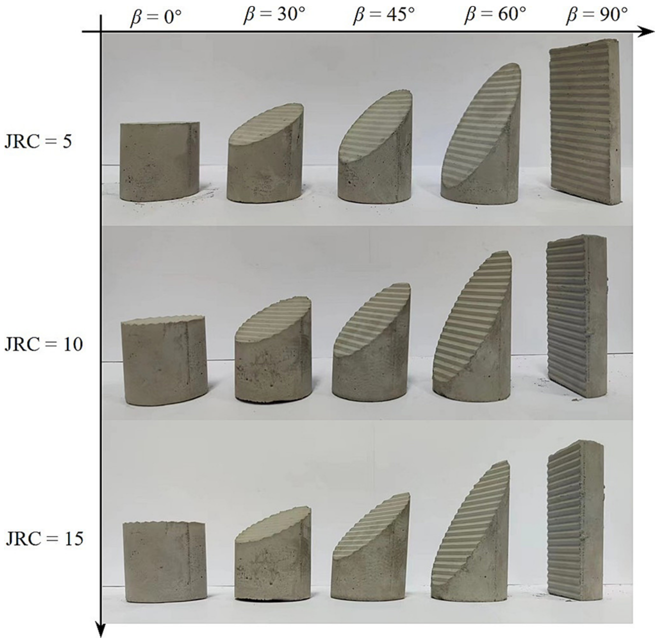

Fig. 5. Semi-jointed specimens.

for each loading condition, with three repeated tests conducted per condition.

In this study, triaxial compression tests were conducted on composite jointed rock mass specimens using the DRTS-500 triaxial testing system at China University of Mining and Technology-Beijing [34]. The axial loading range of the system is 0–500 kN. A displacement-controlled loading mode was adopted, with a loading rate of 0.1 mm/min. Axial deformation was monitored and recorded using a set of linear variable differential transformer (LVDT), whereas radial deformation was monitored via a chain-type displacement sensor. The experimental setup is shown in Fig. 7.

3. Experimental results and analysis

3.1. Mechanical behavior analysis

(1) Stress-strain curves.

Fig. 8 presents the stress-strain curves of the composite jointed rock mass specimens under different working conditions. The curves clearly exhibit similar overall shapes, typically undergoing four stages: compaction, linear elasticity, yield, and failure.

For specimens with joint dip angles of 0°, 30°, and 90°, the post-peak curves become progressively more gradual as the JRC increases, indicating increased ductility. Higher JRC values improve the energy dissipation capacity of the rock mass, making it less susceptible to sudden instability after peak stress. In contrast, specimens with joint dip angles of 45° and 60° exhibit pronounced brittle failure characteristics regardless of the JRC value, with the stress-strain curves sharply dropping after the peak strength is reached.

(2) Elastic modulus and Poisson's ratio.

Fig. 9 presents the experimental results of the elastic modulus and Poisson's ratio of the composite jointed rock specimens under different working conditions.

As shown in Fig. 9a, the variation in the elastic modulus with increasing joint dip angle exhibits a distinct "U"-shaped trend. When the joint dip angle is 0° or 90°, the two matrix sides primarily bear the load, resulting in relatively high elastic modulus values. As the joint dip angle increases, shear-sliding deformation along the joint surfaces becomes more pronounced, thereby reducing the elastic modulus. Moreover, the elastic modulus increases significantly with increasing JRC, particularly for the 0° and 90° specimens, where the increase exceeds 20%. This is attributed to the enhanced interlocking effect of the sawtooth joint surfaces as the JRC increases, which improves the stiffness of the rock mass.

As shown in Fig. 9b, Poisson's ratio initially increases and then decreases with increasing joint dip angle. When the joint dip angle is 0°, the sawtooth joint imposes a significant constraint on the lateral deformation of the specimen. When the joint dip angle ranges from 30° to 60°, the joints act as potential sliding planes for specimen failure, resulting in increased lateral deformation. Additionally, Poisson's ratio decreases gradually with increasing JRC. A greater joint surface roughness enhances the interlocking effect of the sawtooth joints, effectively limiting lateral deformation. When the joint dip angle is 90°, the specimen splits along the joint at the early loading stage, resulting in pronounced lateral deformation. After the separation is completed, subsequent lateral deformation is borne by the two matrix zones on either side and is no longer influenced by the joint.

3.2. Failure mechanism

3.2.1. Failure modes

By observing the variations in specimen failure patterns under different joint dip angles and joint roughness conditions, as

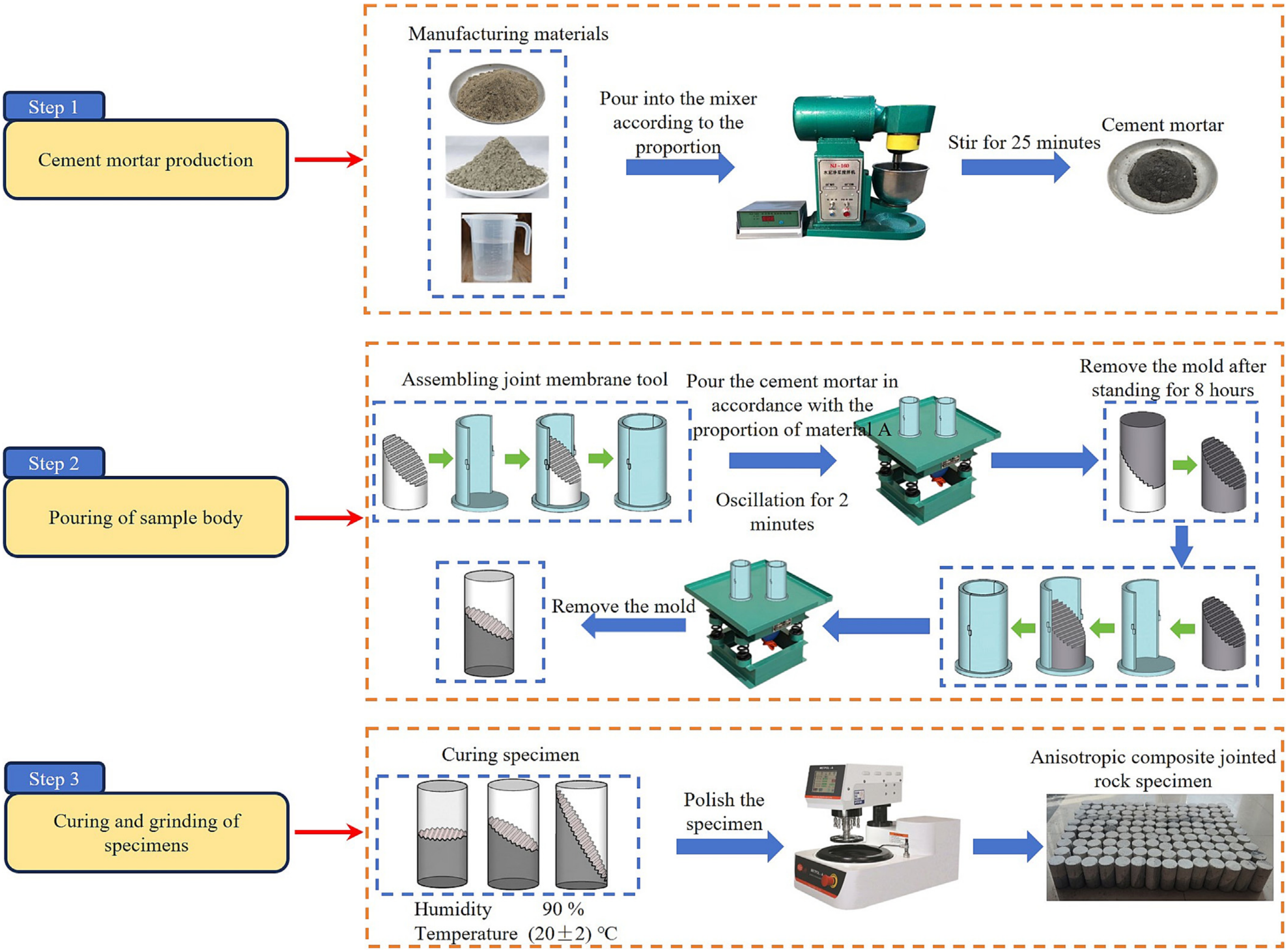

Fig. 6. Fabrication process of composite jointed rock mass specimens.

Table 3
Experimental design scheme.

Joint characteristics								Confining pressure σ_3 (MPa)
Joint roughness coefficient (JRC)			Joint dip angle β (°)					
5	10	15	0	30	45	60	90	8

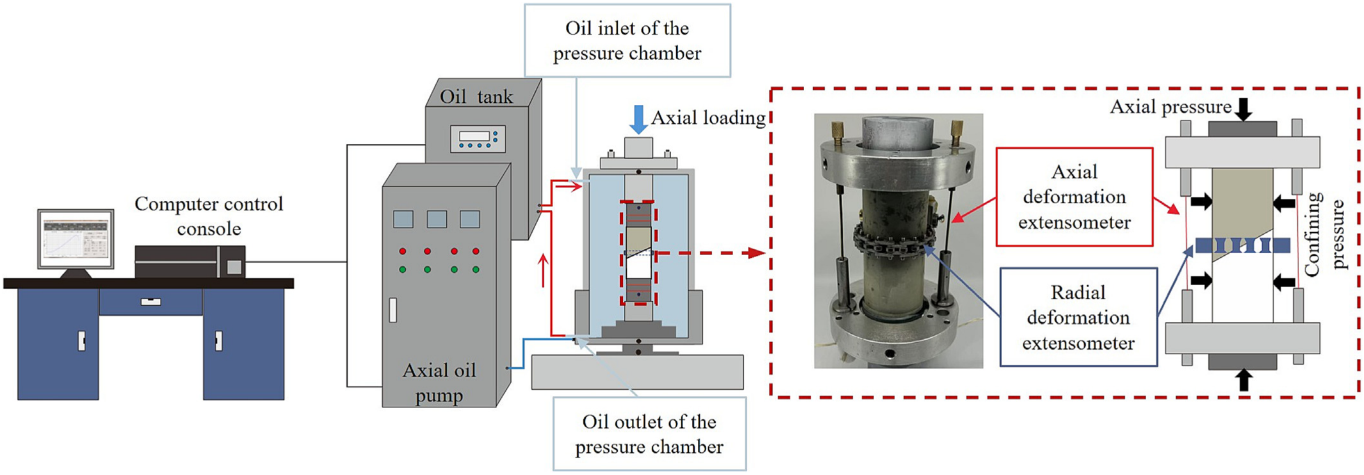

Fig. 7. DRTS-500 triaxial testing system.

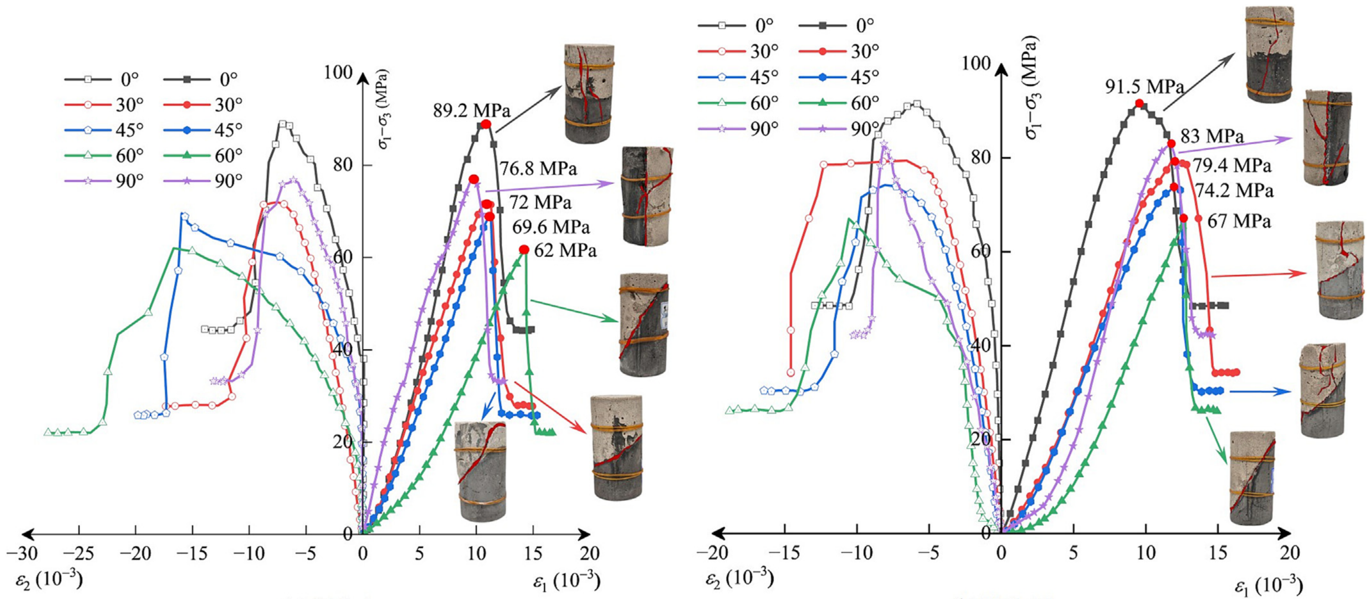

(a) JRC=5

(b) JRC=10

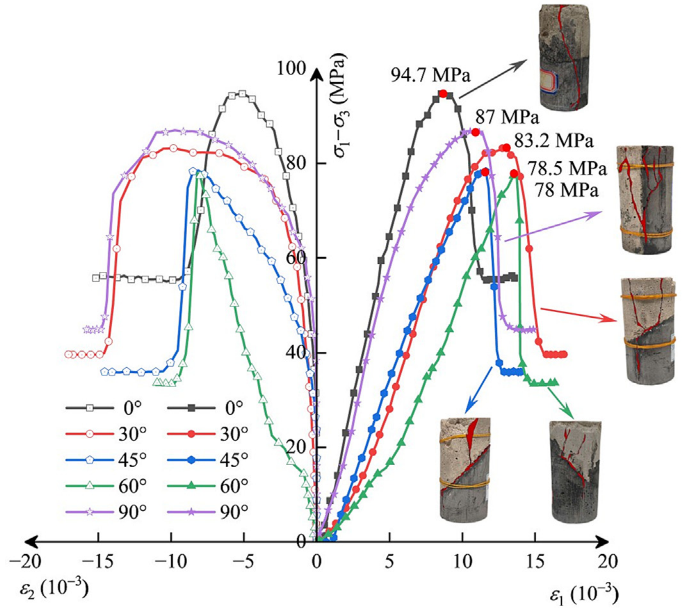

(c) JRC=15

Fig. 8. Stress-strain curves.

shown in Table 4, the failure modes can be categorized into three typical types. These representative failure modes are illustrated in Fig. 10, where the white region represents the weak matrix (Material B), and the dark gray region represents the strong matrix.

(1) Joint failure (JF): As shown in Fig. 10a, this failure mode includes both joint slip failure and joint shear failure, which mainly occur in samples with joint dip angles between 30° and 60° and relatively low joint roughness. The specific failure mode depends on the joint roughness: at a JRC of 5, slip failure dominates, characterized by significant relative displacement along the joint surface with almost no cracks inside the matrix. Under a roughness of 10, shear failure along the joint surface prevails, with evident damage occurring on the joint plane.

(2) Mixed failure (MF): As illustrated in Fig. 10b, this mode results from the combined action of joint failure and matrix failure. Owing to the strength differences between the two matrices, the cracks are denser and more connected on the weaker side, whereas fewer cracks are observed on the stronger side, which is mainly confined near the joint. This mode occurs mainly in specimens with joint dip angles ranging from 30° to 60° and relatively high joint roughness.

(3) Matrix shear failure (MSF): As shown in Fig. 10c, this mode is characterized primarily by shear cracks within the matrix, featuring a through-going fracture penetrating the specimen. Due to the strength difference between the two matrices, cracks are mainly concentrated and first connected on the weaker side, eventually causing overall specimen failure. This mode mainly occurs in specimens with joint dip angles of 0° and 90°.

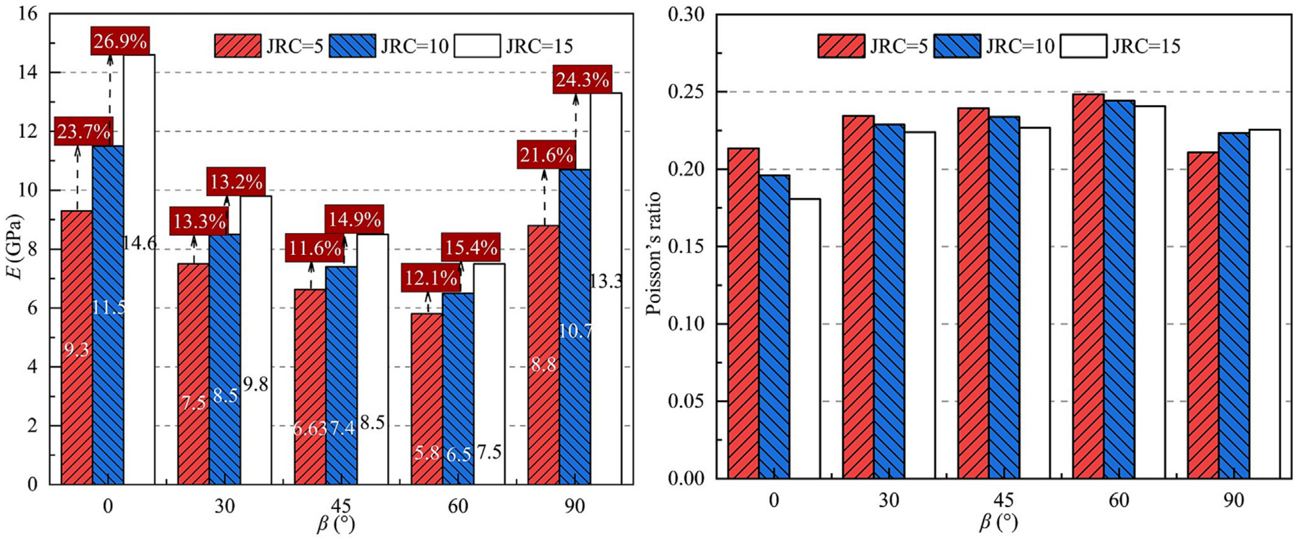

(a) Elastic modulus

(b) Poisson's ratio

Fig. 9. Elastic modulus and Poisson's ratio of jointed specimens with different joint dip angles under the influence of the JRC.

Table 4
Failure photographs of specimens with different joint dip angles and JRC.

Joint roughness coefficient (JRC)	β=0°	β=30°	β=45°	β=60°	β=90°
JRC=5					
JRC=10					
JRC=15					

Table 5 summarizes the failure modes of the composite jointed rock mass specimens under different conditions. The table shows that both the joint dip angle and JRC jointly determine the failure mode of the specimens. Among these factors, the variation of joint dip angle has a decisive influence on the failure mode. When the joint dip angle is 0° or 90°, the specimens exhibit only matrix shear failure, a failure mode minimally affected by the joints, with cracks primarily concentrated in the weaker matrix. When the joint dip angle ranges from 30° to 60°, the influence of joints on the failure mode becomes significantly more pronounced. Specifically, as the joint roughness increases, the failure mode shifts from joint failure to mixed failure.

3.2.2. Failure mechanism

This study focuses on the stress state at the joint located at the specimen center to investigate the influence of joint geometric characteristics on specimen strength and to reveal the failure mechanism of composite jointed rock masses.

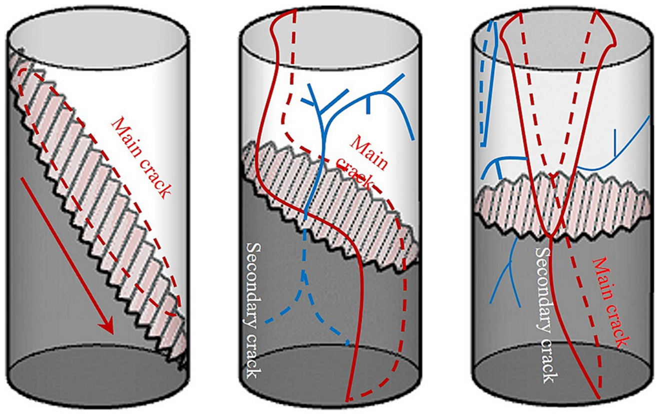

(a) JF (b) MF (c) MSF

Fig. 10. Failure modes.

This study conducts a stress analysis at the center of the specimen, as illustrated in Fig. 11. The detailed analysis is as follows:

(1) When the joint dip angle is 0°, the joint surface is perpendicular to the principal stress direction, and the joint surface is under compression. Under the action of axial deviatoric stress, the specimen tends to undergo radial deformation. Influenced by this tendency, the sawtooth joint surface generates shear resistance under normal stress, which inhibits the radial deformation of the specimen. The normal stress and shear stress acting on the center point of the joint surface can be expressed as:

$$\begin{cases} \sigma_{\mathrm{n}} = \sigma_1 \\ \tau_{\mathrm{s}} = 0 \end{cases} \tag{3}$$

At this time, the shear resistance of the joint generated by the normal stress on the joint surface is calculated as follows:

$$\tau_{\mathrm{j}} = \sigma_0 \tan(\varphi + i) + C \tag{4}$$

where φ represents the internal friction angle of the joint surface; and i the asperity angle of the joint surface. Obviously, the shear strength of the sawtooth joint is significantly greater than that of a planar joint. The sawtooth joint restricts radial displacement at the joint surface, preventing shear failure along the joint. For specimens with a joint dip angle of 0°, a “thicker at both ends and thinner in the middle” deformation pattern is observed after failure, where deformation at the specimen ends is significantly greater than that at the joint location. This phenomenon confirms the aforementioned conclusion.

(2) When the joint dip angle is 90°, the joint surface is parallel to the direction of the principal stress. The normal stress and shear stress acting on the joint surface are expressed as shown in Eq. (5):

$$\begin{cases} \sigma_{\mathrm{n}} = \sigma_3 \\ \tau_{\mathrm{s}} = 0 \end{cases} \tag{5}$$

At this point, the normal stress acting on the joint is tensile. There is no shear stress along the joint surface, and the entire joint is under tensile stress. The tensile strength of the joint is provided by the joint bonding strength, which is relatively low and significantly weaker than the strength of the surrounding matrix. As a result, tensile failure occurs along the joint. However, due to the presence of confining pressure, the specimen does not completely fail after cracking along the joint; the lateral deformation is constrained, which suppresses further crack propagation. Under these conditions, the strength of a specimen is determined primarily by the strength of the matrix on both sides rather than by the tensile strength of the joint itself. Therefore, the matrix strength becomes the decisive factor in the failure of the specimen. Nevertheless, although matrix failure governs the final failure mode, the overall strength of the specimen remains lower than that of the matrix. This is attributed to the change in aspect ratio of the matrix blocks on either side; as the aspect ratio increases, the specimen strength decreases.

(3) When the joint dip angle is between 30° and 60°, the normal stress and shear stress on the joint surface can be calculated by Eq. (6):

$$\begin{cases} \sigma_{\mathrm{n}} = \frac{\sigma_1 + \sigma_3}{2} + \frac{\sigma_1 - \sigma_3}{2} cos2\beta \\ \tau_{\mathrm{s}} = \frac{\sigma_1 - \sigma_3}{2} sin2\beta \end{cases} \tag{6}$$

At this point, the sawtooth joint is subjected to normal stress, which generates shear resistance along the joint surface. The shear resistance of the joint can be calculated via the following equation:

$$\begin{aligned} \tau_{\mathrm{j}} &= \sigma_{\mathrm{n}} \tan(\varphi + i) + C \\ &= \left(\frac{\sigma_1 + \sigma_3}{2} + \frac{\sigma_1 - \sigma_3}{2} \cos 2\beta\right) \tan(\varphi + i) + C \end{aligned} \tag{7}$$

The difference between the shear stress at the center point of the joint surface and the joint shear strength is defined as $\Delta\tau$:

$$\begin{aligned} \Delta\tau &= \tau_{\mathrm{s}} - \tau_{\mathrm{j}} \\ &= \frac{\sigma_1 - \sigma_3}{2} (\sin 2\beta - \cos 2\beta \tan(\varphi + i)) - \frac{\sigma_1 + \sigma_3}{2} \tan(\varphi + i) - C \end{aligned} \tag{8}$$

Fig. 12 shows the variation of shear stress at the joint surface of the specimen within the dip angle range of 30°–60°, under a principal stress of 50 MPa.

When $\Delta\tau$ is greater than 0, the shear stress at the center of the joint surface exceeds the joint’s shear strength, causing shear failure at the joint. However, $\Delta\tau>0$ does not necessarily mean that the specimen undergoes overall shear failure along the entire joint. According to previous research [35], as the distance from the joint center increases, the shear stress generated by the axial force gradually decreases. This results in $\Delta\tau$ at the center being significantly higher than at the edges, meaning that failure occurs at the joint center while the ends remain intact. In this case, the failure mode of the specimen is classified as mixed failure.

As the joint dip angle increases, $\Delta\tau$ gradually increases, indicating that the likelihood of shear failure occurring along the joint also increases. This is because, with increasing dip angle, the shear stress acting on the joint surface continuously increases, causing $\Delta\tau$ at the joint edges to increase as well. When $\Delta\tau$ at the edges becomes greater than 0, the entire joint undergoes shear failure, and the corresponding failure mode is classified as joint failure.

Table 5
Summary of failure modes of composite jointed rock specimens.

Joint roughness coefficient (JRC)	Joint dip angle β				
	β=0°	β=30°	β=45°	β=60°	β=90°
5	MSF	JF	JF	JF	MSF
10	MSF	MF	MF	JF	MSF
15	MSF	MF	MF	MF	MSF

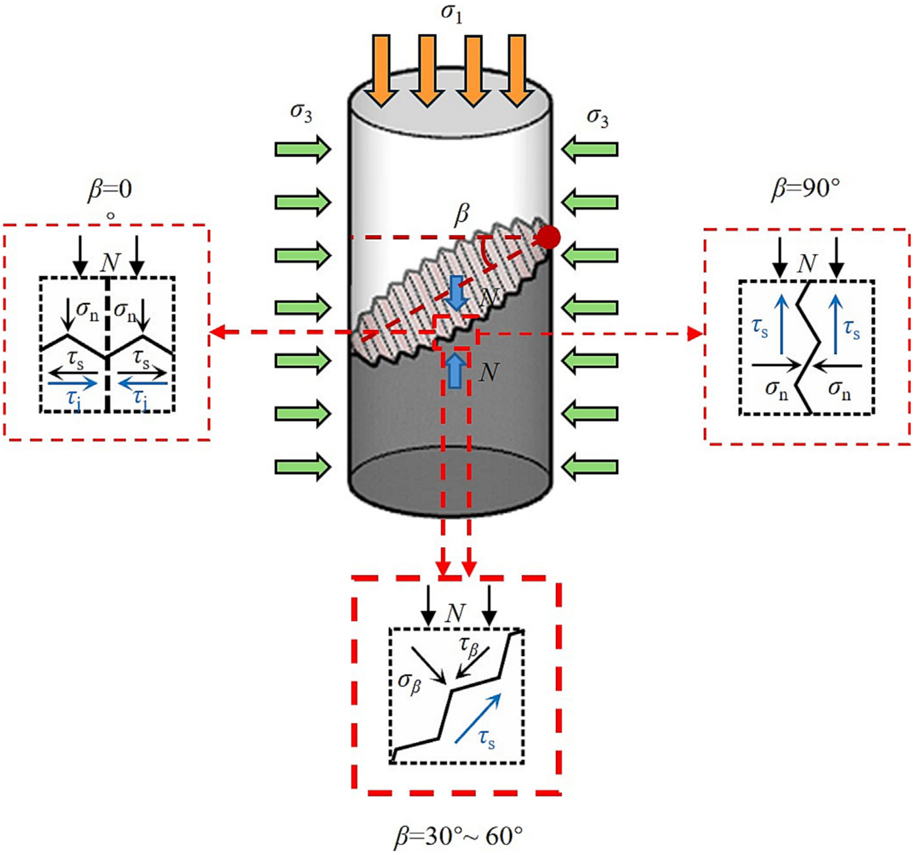

Fig. 11. Schematic diagram of stress analysis at the center of composite jointed specimen.

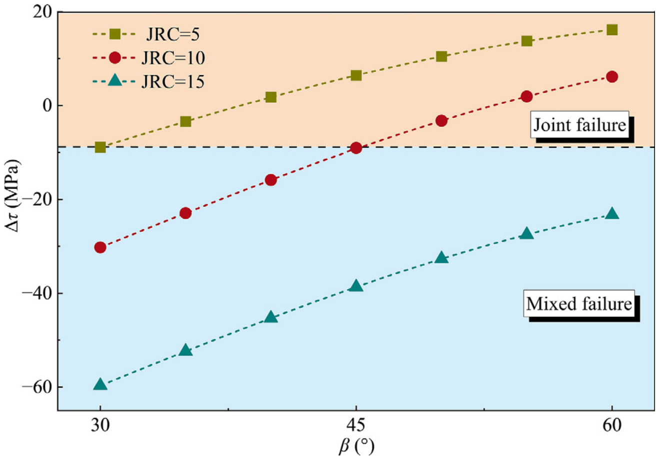

Fig. 12. Variation of shear stress at the center of joints in specimens with different joint dip angles.

Within the joint dip angle range of 30°–60°, the joint roughness significantly affects the failure mode of the specimen. As the joint roughness increases, the shear strength of the joint surface increases, allowing the specimen to withstand higher shear stress during loading, thereby increasing the difficulty of shear failure occurrence. However, it is important to note that even when $\Delta\tau$ is less than 0, it does not mean that the joint surface will not experience any failure. Due to the serrated shape of the joint, stress concentration occurs at the corners of the serrations. Therefore, even if the resultant shear stress is relatively low, there is still a possibility of failure. In such cases, localized failure may occur on the joint surface.

Based on the above analysis, the failure mode of the specimen is jointly influenced by the joint dip angle and joint roughness, with the joint dip angle being the decisive factor. The failure mechanisms of composite joint specimens can be specifically explained as follows:

(1) When the joint dip angle is 0° or 90°, the failure mode of the specimen is matrix shear failure.

At 0°, the joint surface of the composite joint specimen is under compression. Under this condition, the sawtooth joint is compressed, significantly enhancing the interlocking effect between joint surfaces, effectively restricting the lateral deformation of the specimen and increasing its resistance to deformation and failure. When the external load exceeds the strength of the weaker matrix side, failure occurs, and the failure strength is essentially determined by the strength of the weakened matrix reinforced by the sawtooth joint. At 90°, the failure mode is similar to that at 0°, mainly matrix shear failure, but the joint surface in the 90° specimen tends to be penetrated.

(2) When the joint dip angle is between 30° and 60°, the stress state at the joint center is more complex than that at 0°. At this stage, the joint is under combined compression and shear, and the specimen can exhibit two different failure modes:

Joint failure: This failure typically occurs at relatively high joint dip angles and low joint roughness. At higher dip angles, the compressive stress at the joint is relatively small, whereas the shear stress is large, making the joint surface prone to shear failure.

Mixed failure: As the joint strength increases, the failure mode gradually transitions from joint failure to mixed failure. Increased joint roughness and decreased joint dip angle help improve the joint shear strength, increasing the difficulty of joint failure. When the difference between the joint strength and the weaker matrix strength decreases to a certain level, failure is no longer limited to the joint but also induces damage within the matrix. Additionally, due to the stress concentration at the serration tips, local damage may also occur on the joint surface. At this stage, the failure mode is mixed failure.

3.3. Strength parameters

(1) Peak strength.

Fig. 13 presents the experimental results of the peak strength of composite jointed rock masses under different conditions. The peak strengths of the specimens exhibits a "U"-shaped trend with increasing joint dip angle, initially decreasing and then increasing. When the joint dip angle is 0° or 90°, the strength of the jointed rock mass is relatively high, primarily controlled by the strength of the rock matrix material, with minimal influence from the joint surfaces. As the joint dip angle increases to between 30° and 60°, the weakening effect of the joint surface becomes more significant, and the peak strength gradually decreases. Notably, at a joint dip angle of 60°, the specimens have the lowest strength, indicating the poorest mechanical stability and the highest susceptibility to failure under these conditions. Furthermore, the peak strength of the specimens increases with increasing JRC. This is mainly because a higher JRC enhances the interlocking and self-locking effects of the sawtooth joints, thereby further increasing the peak strength of the jointed rock mass.

An analysis of the correspondence between failure mode and strength revealed that the failure mode transitions from matrix shear failure to joint failure and mixed failure as the joint dip angle increases, and the failure mode eventually returns to matrix shear failure. For specimens exhibiting joint failure, the primary cause is that the shear stress on the joint surface exceeds the shear strength of the joint, which is significantly lower than the strength of the weaker matrix. When the failure mode shifts to mixed failure, the combined action of the joint surface and the weaker matrix leads to specimen failure. For specimens failing by matrix shear failure, the joints have negligible influence, and the joint surfaces no longer represent weak points; the specimen strength is governed entirely by the matrix.

(2) Analysis of strength anisotropy.

As shown in the above strength analysis, the specimens exhibit pronounced anisotropy in strength. In previous studies [36], the anisotropy index of strength, $\lambda_\sigma(\beta)$, was adopted to quantitatively evaluate the effect of joint roughness on the anisotropy of the specimens. The calculation is given in Eq. (9).

$$\lambda_\sigma(\beta) = \frac{\sigma_0 - \sigma_\beta}{\sigma_0} \times 100\% \tag{9}$$

where σ_0 is the specimen strength at a joint dip angle of 0°; and σ_β the specimen strength under the same conditions at a joint dip angle of β. A higher anisotropy index indicates a more pronounced anisotropic behavior of the specimen's strength and greater strength variation across different joint dip angles.

Fig. 14 presents the variation of the anisotropy index of specimens with different joint roughness values as a function of joint dip angle. The anisotropy index first increases and then decreases with increasing joint dip angle, reaching its peak at 60°, where the strength disparity among specimens is the greatest. With increasing joint roughness, the variation in specimen strength across different joint dip angles gradually diminishes. This is attributed to the significant increase in the joint shear strength due to higher roughness, which reduces the strength contrast between the joint plane and the matrix. As a result, the influence of the joint on the overall strength of the specimen weakens, leading to a decrease in the strength anisotropy.

(3) Damage stress parameters.

The crack initiation stress (σ_{ci}) and crack damage stress (σ_{cd}) are currently the primary characteristic parameters used to assess rock damage. This section adopts the calculation methods of the crack initiation stress and expansion stress proposed by Zhang et al. [37]:

$$\varepsilon_{ve} = \frac{1-2\mu}{E}(\sigma_1+\sigma_2+\sigma_3) \tag{10}$$

In this equation, E and μ represent the elastic modulus and Poisson's ratio of the specimen, respectively. Since the type of triaxial test used in this study is a conventional triaxial compression test, the method for calculating the volumetric strain of the cracks is as follows:

$$\varepsilon_{vc} = \varepsilon_v - \varepsilon_{ve} \tag{11}$$

Based on the above two equations, the calculated elastic volumetric strain and crack volumetric strain of the composite jointed specimen 0°–10 (The specimen was designated in the β–JRC format) were plotted on the corresponding deviatoric stress-strain curves (Fig. 15.). Considering that the peak strengths vary among

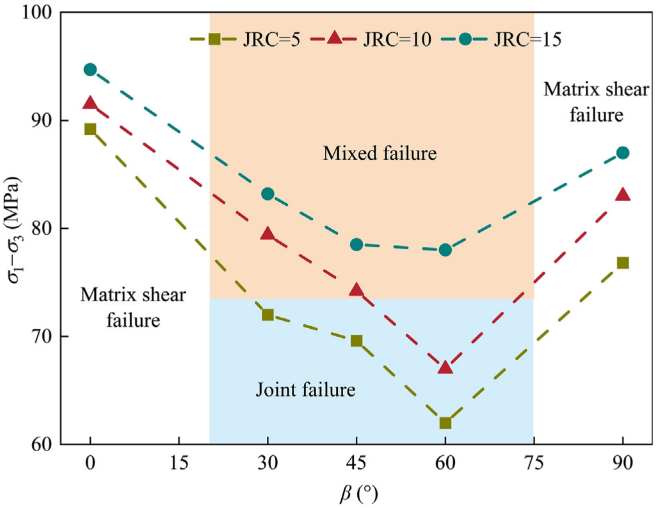

Fig. 13. Peak strength curves of jointed specimens with different joint dip angles under the influence of JRC.

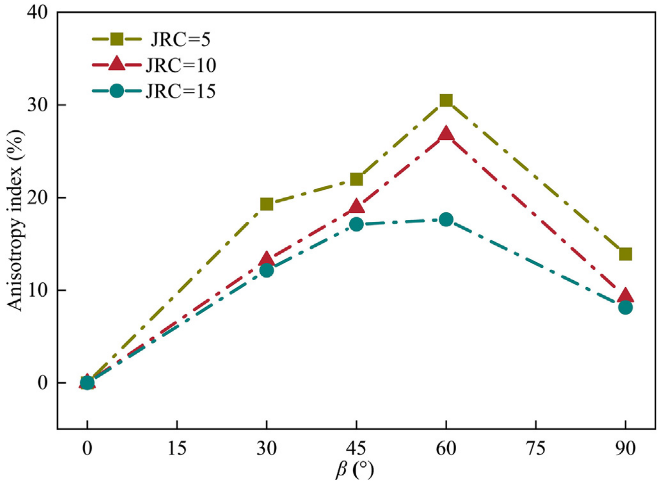

Fig. 14. Anisotropy index variation of specimens with different joint roughness versus joint dip angles.

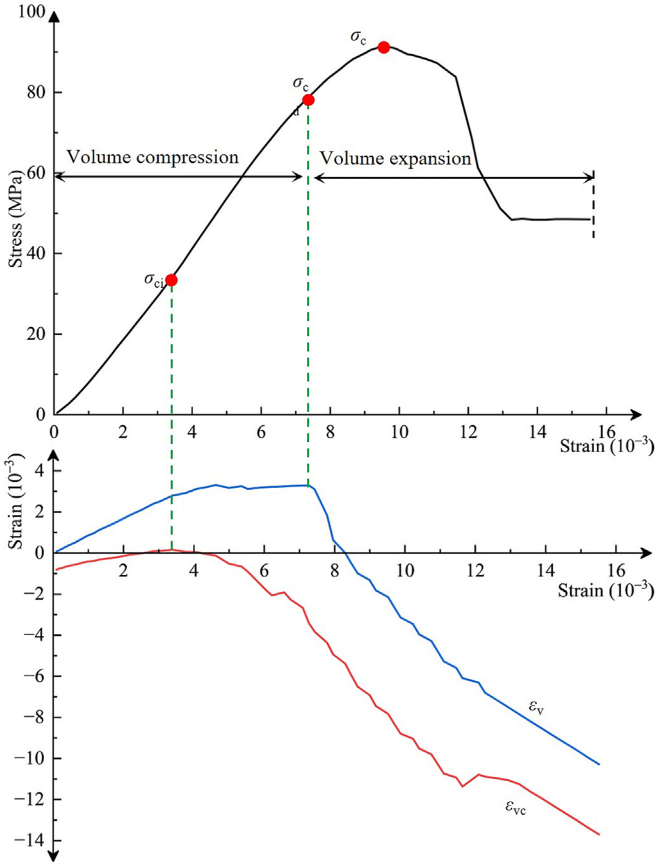

Fig. 15. Schematic diagram of the determination of damage stress parameters for composite jointed rock specimens.

different specimens, directly comparing the magnitudes of crack initiation stress and crack damage stress alone cannot accurately reflect the influence of joint surface characteristics on the damage stress of composite jointed rock specimens. Therefore, the damage stress values were normalized using the peak stress of each specimen as the reference. Table 6 presents the results for elastic volumetric strain, crack volumetric strain, and normalized crack volumetric strain for different specimens.

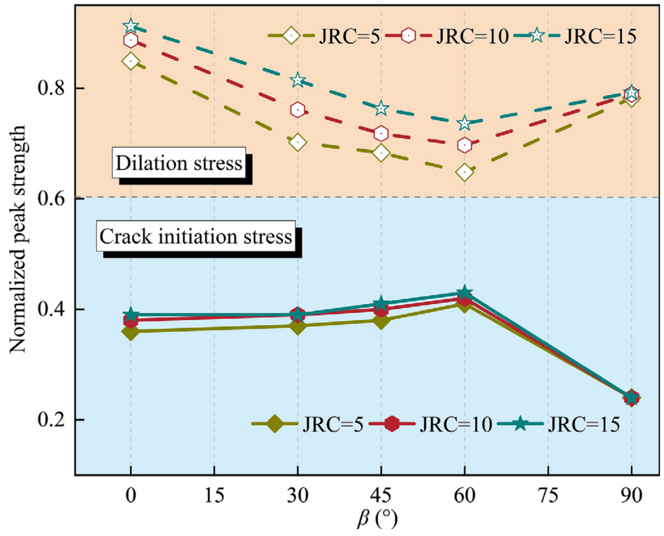

Fig. 16. Influence of joint characteristics and displacement on normalized damage stress parameters of specimens.

Fig. 16 shows the variation of normalized characteristic stresses of composite jointed rock specimens with JRC under different joint dip angles. As shown in the figure, the joint dip angle has a decisive influence on the damage stress parameters of the specimens. For the crack initiation stress, with the exception of 90°, the normalized crack initiation stress shows little variation with JRC for other joint dip angles. This indicates that the compaction and elastic deformation stages occupy a similar proportion of the entire loading process for these specimens. However, the crack initiation stress is significantly lower in the specimens with a 90° joint dip angle than in those with other joint dip angles. This is because specimens with a 90° inclination tend to separate along the joint under relatively low external loads, reducing the proportion of the compaction and elastic deformation stages during loading.

The dilation stress tends to decrease and then increase with increasing joint dip angle. Joint roughness also influences the damage stress parameters, particularly the dilation stress, whereas its effect on the crack initiation stress is negligible. Increased joint roughness significantly enhances the shear strength of the joints, thereby delaying specimen failure. However, when the joint dip angle is 90°, the effect of roughness on the dilation stress is minimal. This is because increased roughness only enlarges the joint contact area, which has a limited effect on the joint strength and therefore does not significantly influence the dilation stress of the specimen.

Table 6
Damage stress parameters and normalized damage stress of composite jointed rock specimens.

Specimen number	Volume compression		Volume expansion		Peak strength σ_c (MPa)
	Cracking stress σ_{ci} (MPa)	σ_{ci}/σ_c	Dilatancy stress σ_{cd} (MPa)	σ_{cd}/σ_c	
0°–5	31.84	0.36	75.73	0.85	89.2
30°–5	26.35	0.37	50.54	0.70	72
45°–5	26.59	0.38	47.54	0.68	69.6
60°–5	25.36	0.41	40.18	0.65	62
90°–5	18.05	0.24	60.06	0.78	76.8
0°–10	34.59	0.38	81.16	0.89	91.5
30°–10	30.73	0.39	60.42	0.76	79.4
45°–10	29.61	0.40	53.28	0.72	74.2
60°–10	28.07	0.42	46.70	0.70	67
90°–10	19.84	0.24	65.49	0.79	83
0°–15	37.03	0.39	86.37	0.91	94.7
30°–15	32.78	0.39	67.72	0.81	83.2
45°–15	32.34	0.41	59.90	0.76	78.5
60°–15	33.77	0.43	57.41	0.74	78
90°–15	21.14	0.24	68.90	0.79	87

Gao et al. [38] indicated that the stage from crack initiation stress to dilation stress can be defined as the unstable crack development phase. The proportion of this phase is defined as the crack unstable development ratio (CUDR), which is calculated by the following equation:

$$CUDR = \frac{\sigma_{\mathrm{cd}} - \sigma_{\mathrm{ci}}}{\sigma_{\mathrm{c}}} \times 100\% \tag{12}$$

A lower CUDR indicates that a specimen undergoes rapid accumulation of internal damage within a short time, making the precursors to failure less obvious and making the specimen more brittle. Fig. 17 shows the variation of CUDR with increasing joint dip angle under different joint roughness conditions. When the joint plane is inclined, the proportion of the crack development phase is significantly lower than that of specimens with joint dip angles of 0° and 90°, indicating that the specimens with inclined joints are significantly more brittle than those with 0° and 90° joints. Furthermore, the brittleness increases noticeably with increasing joint dip angle. Additionally, an increase in joint roughness increases the CUDR, thereby reducing the brittleness of the specimen.

3.4. Energy characteristics

(1) Energy evolution process.

The failure of rock and rock-like materials is essentially an energy-driven instability phenomenon, which involves both the accumulation and release of internal energy. The stored energy is manifested as elastic energy, whereas the dissipated energy is released through plastic deformation, damage, and fracture mechanisms [39]. It is assumed that during the loading process, apart from the external input energy, the specimen does not exchange heat with the external environment. The testing system satisfies the following conditions:

$$U = U_{\mathrm{d}} + U_{\mathrm{e}} \tag{13}$$

where U_{d} and U_{e} represent the dissipated energy and the elastic energy stored within the specimen during the loading process, respectively; and U the total energy input into the specimen. Fig. 18 shows a schematic diagram of these two types of energy.

Since the triaxial loading method used in this study is the conventional triaxial loading method, it follows that $\sigma_2=\sigma_3$ and $\varepsilon_2=\varepsilon_3$.

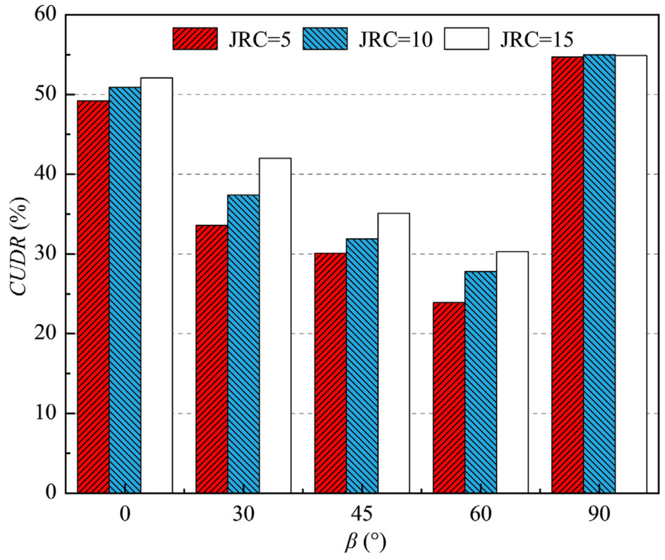

Fig. 17. Effect of joint roughness on the CUDR.

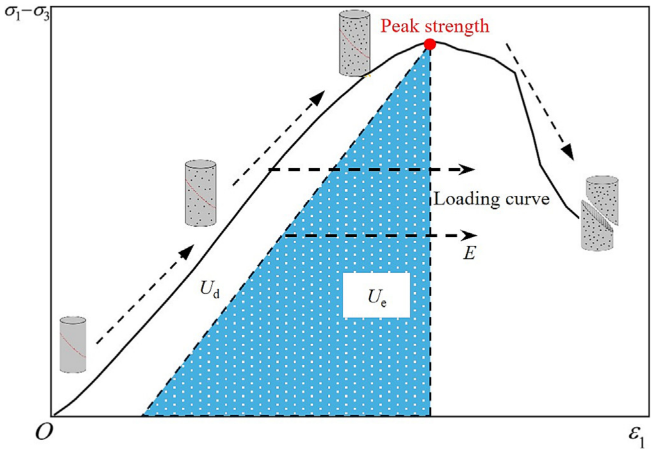

Fig. 18. Schematic diagram of energy components.

Therefore, the energy calculation method in the above figure is as follows:

$$\begin{cases} U = \int_0^{\varepsilon_1} \sigma_1 \mathrm{d}\varepsilon_1 + 2\int_0^{\varepsilon_3} \sigma_3 \mathrm{d}\varepsilon_3 \\ U_{\mathrm{e}} = \frac{1}{2E}\left[\sigma_1^2 + 2\sigma_3^2 - 2\mu(2\sigma_1\sigma_3 + \sigma_3^2)\right] \\ U_{\mathrm{d}} = U - U_{\mathrm{e}} \end{cases} \tag{14}$$

where E and μ represent the elastic modulus and Poisson's ratio of the jointed specimen, respectively.

Due to space limitations, the energy evolution curves of the composite jointed specimens (numbered 0°–10) are plotted in Fig. 19 and divided into four stages: Stage I: initial compaction stage—the total energy, elastic energy, and dissipated energy of the jointed specimen all increase with increasing axial strain, whereas the dissipated energy remains at a relatively low level throughout this stage. Stage II: elastic deformation stage—the deformation of the specimen is predominantly elastic. The elastic energy increases rapidly, and the dissipated energy remains nearly unchanged. Stage III: Crack propagation stage—significant internal damage occurs within the specimen. The accumulation rate of elastic energy clearly decreases, whereas the dissipated energy increases significantly. Stage IV: Final failure stage—rapid failure occurs within the specimen. The stored elastic energy is largely released and transformed into dissipated energy, which is consumed during crack extension and fracture, ultimately leading to the global instability and failure of the specimen.

(2) Elastic energy analysis.

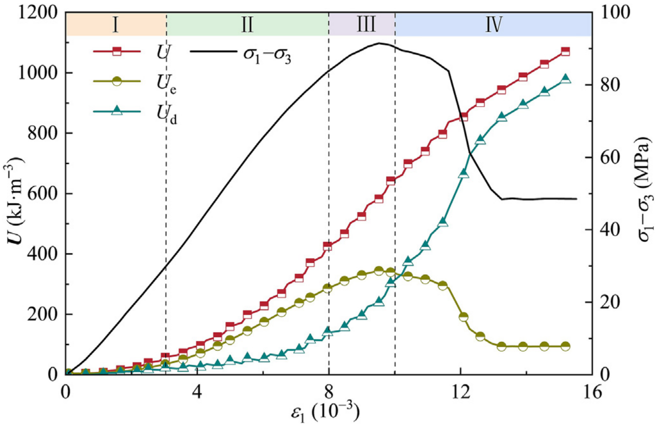

Fig. 19. Energy evolution curves of composite jointed specimen 0°–10.

To investigate the influence of joint dip angle on the elastic energy of jointed rock masses, Fig. 20 presents the variation curves of the elastic energy with the joint dip angle under different joint roughness conditions. Under all roughness conditions, the elastic energy exhibits a distinct "U-shaped" trend with increasing joint dip angle. When the joint dip angle is 0°, the joint plane is perpendicular to the loading direction. The strong confinement effect of the joint plane results in higher specimen stiffness during loading, allowing for greater storage of elastic energy. As the joint dip angle increases (within the range of 30°–60°), the shear strength of the joint plane decreases, making it more susceptible to slip failure. Consequently, the load-bearing capacity of the specimen decreases, leading to a significant reduction in elastic energy. When the joint dip angle reaches 90°, the joint plane becomes parallel to the loading direction. In this case, the influence of the joint plane on the overall strength of the specimen decreases, resulting in a recovery of the load-bearing capacity and a corresponding increase in the elastic energy. Moreover, an increase in joint roughness noticeably enhances the elastic energy. A rougher joint surface provides greater interlocking, which improves the overall stiffness of the specimen and enhances its capacity to store elastic energy.

(3) Dissipated energy analysis.

Fig. 21 presents the fitting curves of strength versus dissipated energy under different failure modes.

When the specimen fails in a matrix shear failure mode (Fig. 21a), the relationship between the strength and dissipated energy is most pronounced. As the strength increases, the dissipated energy also increases significantly, with a fitted slope of 3.57, indicating a strong linear correlation. This suggests that in this mode, higher specimen strength leads to greater energy consumption during crack propagation and deformation.

When the specimen exhibits a mixed failure mode (Fig. 21b), the fitted slope is 3.11, and the correlation between the strength and dissipated energy is weaker than that of the matrix shear failure mode. Mixed failure typically involves both joint slippage and matrix shearing. Since joint slippage consumes significantly less energy than matrix failure does, the increase in dissipated energy resulting from increased strength is limited by the relatively low energy demand of joint failure, leading to a smaller overall increase.

For joint-dominated failure (Fig. 21c), although a positive correlation still exists between strength and dissipated energy, the fitted slope decreases significantly to only 1.76. This is because this mode is primarily controlled by joint failure, which requires far less energy than matrix failure does, thereby resulting in substantially lower dissipated energy.

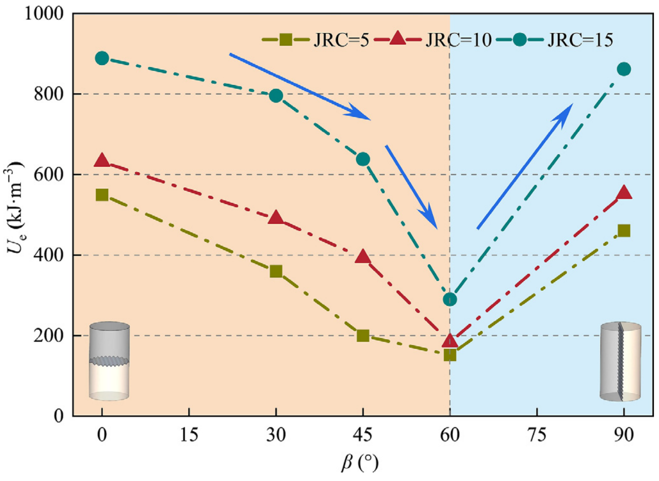

Fig. 20. Variation of elastic energy of jointed specimens with joint dip angle.

(4) Linear energy storage law.

The linear energy storage law has been increasingly applied in conventional uniaxial and triaxial tests of intact rocks [40–42]. However, whether this law is applicable to jointed rock specimens requires further investigation. According to the linear energy storage law, the total energy, strain energy, and dissipated energy of the specimen exhibit clear linear relationships, expressed as follows:

$$\begin{cases} U_{\mathrm{e}} = A \cdot U + B \\ U_{\mathrm{d}} = (1 - A) \cdot U - B \end{cases} \tag{15}$$

In Fig. 22, the characteristic energies of composite jointed rock specimens under different failure modes are fitted according to the above equation. As shown, composite jointed specimens under the same failure mode follow the linear energy storage law. The goodness of fit for failure modes dominated by matrix shear failure and joint failure is significantly greater than that for mixed failure, indicating that the more singular the failure mechanism, the better the applicability of the linear energy storage law. A larger value of A indicates a better energy storage capacity and greater strength of the specimen, whereas a smaller A value suggests that the specimen is more prone to energy dissipation and release during loading, implying a greater failure potential. The A values corresponding to matrix failure, mixed failure, and joint-controlled failure decrease successively, indicating a gradual reduction in the energy storage capacity. This trend demonstrates that specimens dominated by joint-controlled failure are more susceptible to instability. Therefore, in practical engineering applications, special attention should be given to rock masses with well-developed joints and joint-controlled failure mechanisms. Appropriate support and protective measures should be implemented to reduce the risk of failure in such regions.

(5) Characteristic energy.

The unit release rates of elastic energy and dissipated energy are commonly defined as the energy release rate (G_{e}) and energy dissipation rate (G_{d}), respectively. They are calculated as follows:

$$\begin{cases} G_{\mathrm{e}} = \frac{\partial U_{\mathrm{e}}}{\partial \varepsilon} \\ G_{\mathrm{d}} = \frac{\partial U_{\mathrm{d}}}{\partial \varepsilon} \end{cases} \tag{16}$$

The energy release rate and energy dissipation rate characterize the instantaneous accumulation and dissipation of energy within the specimen. The ratio of the two serves as an indicator of the specimen's stability, and this ratio is defined as the characteristic energy:

$$\chi = \frac{G_{\mathrm{e}}}{G_{\mathrm{d}}} \tag{17}$$

Fig. 23 illustrates the variation curves of χ during loading for the composite jointed specimen 60°–10. As shown in the figure, χ initially increases and then decreases. Before χ starts to decrease, the energy storage mechanism dominated by elastic energy plays a leading role in the deformation process of the rock. Once χ begins to decrease, the weakening effect led by energy dissipation becomes dominant. This inflection point typically corresponds to the specimen's dilation stress. The peak characteristic energy under different joint roughness are plotted in Fig. 24. The peak characteristic energy can reflect the brittleness of the specimen. For specimens with higher brittleness, only a small portion of the energy is converted into dissipation before entering the stage of unstable crack propagation, resulting in a high proportion of elastic energy. After the external load exceeds the dilation stress, the specimen enters the unstable crack propagation phase, where dissipated energy becomes dominant. Such specimens exhibit strong

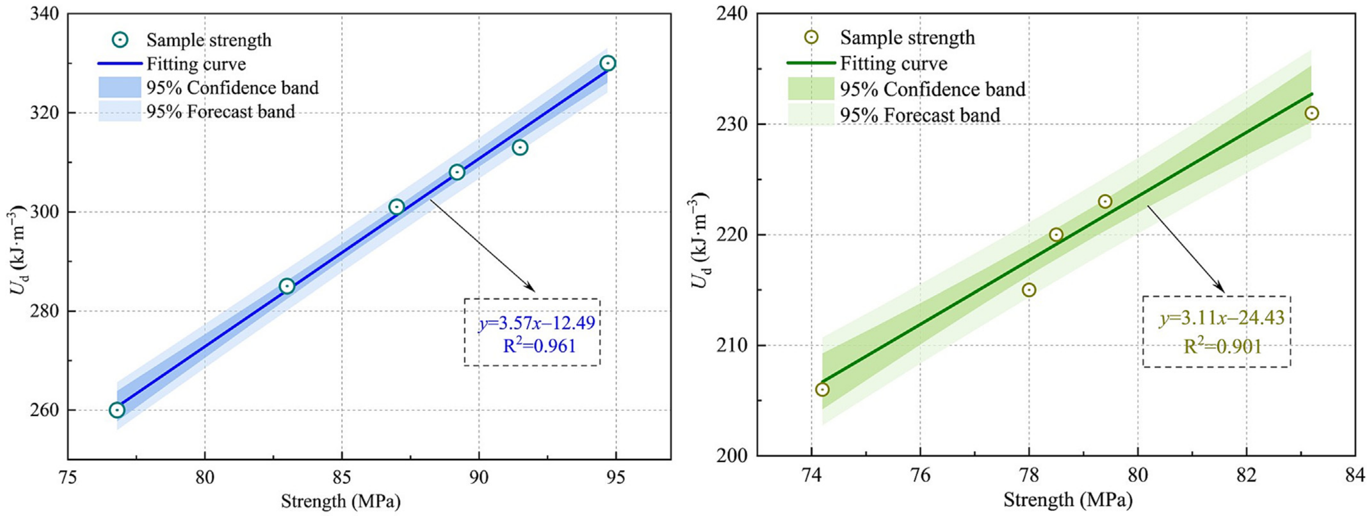

(a) Matrix shear failure

(b) Mixed failure

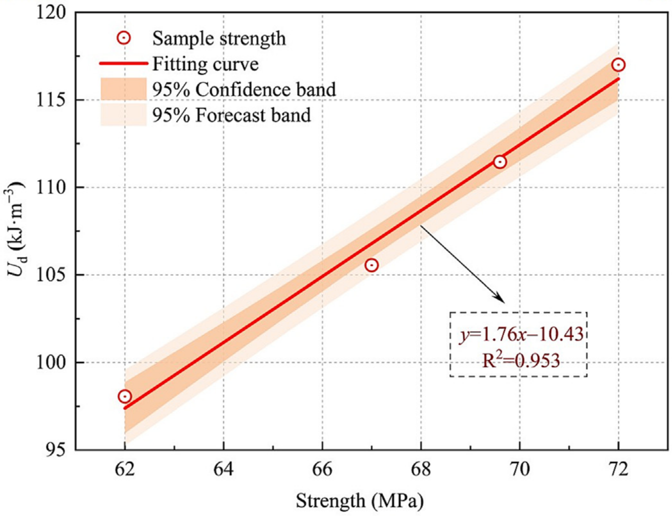

(c) Joint failure

Fig. 21. Relationships between strength and dissipated energy under different failure modes and their fitting curves.

energy accumulation capacity and weak energy dissipation during the stable phase. In contrast, specimens with lower brittleness already convert a certain amount of energy into dissipation during the stable phase, leading to poorer energy accumulation and stronger dissipation capacity. It is manifested as the peak value of χ being smaller than that of brittle rocks.

4. Mesoscopic damage evolution analysis

4.1. Model establishment

This study employs the well-established discrete element method (DEM) numerical simulation software PFC2D (Particle Flow Code in 2 Dimensions) to conduct numerical simulations of heterogeneously composite jointed rock masses.

The specific modeling procedure is as follows:

(1) Base model generation: Random particles with radii ranging from 0.1 to 0.3 mm are generated within a predefined domain. After reaching static equilibrium, a specimen of appropriate dimensions is extracted (the triaxial compression model is a rectangle with a height of 100 mm and a width of 50 mm).
(2) Joint importation: The joint geometry drawn in AutoCAD is imported into the model. The model is then divided into three regions: the joint zone, the strong matrix side, and the weak matrix side.
(3) Assignment of regional parameters.
(4) Loading conditions: A flexible membrane servo mechanism is employed to apply the confining pressure, which is set to 8 MPa. Axial loading is applied through displacement control at a rate of 10^{-5} mm/s to ensure quasi-static loading conditions.

The model construction process is illustrated in Fig. 25.

4.2. Selection of mesoscopic parameters and validation of their reasonableness

4.2.1. Selection of mesoscopic parameters

Based on the peak strength, elastic modulus, and other mechanical parameters obtained from laboratory tests on jointed rock-like specimens, a trial-and-error method was employed to continuously adjust the mesoscopic parameters required for numerical simulation. The finalized parameters are presented in Table 7.

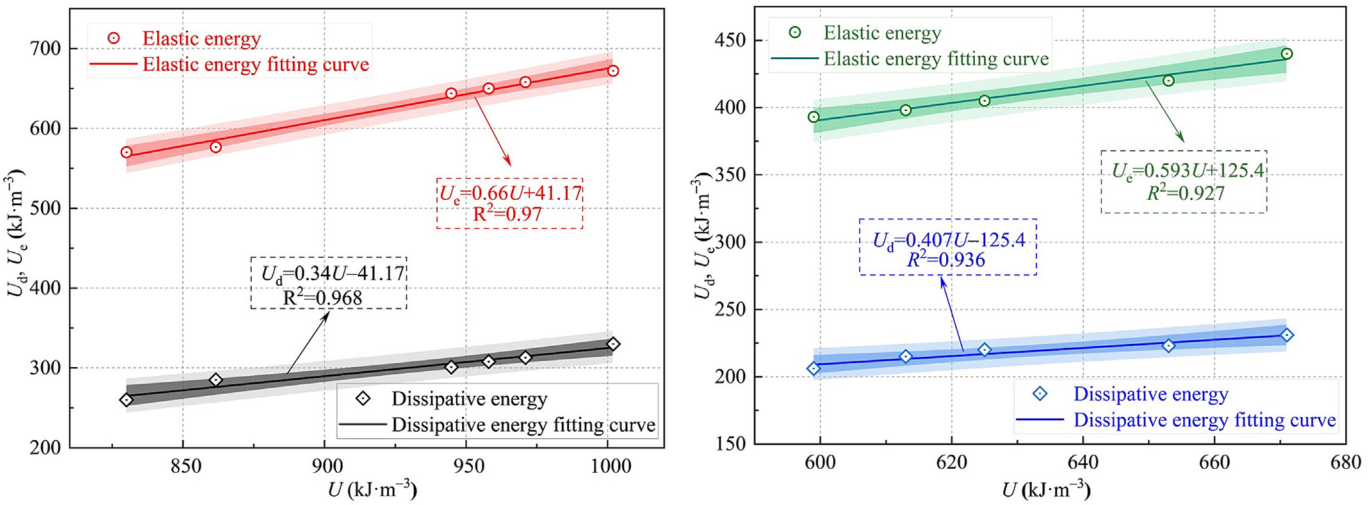

(a) Matrix shear failure

(b) Mixed failure

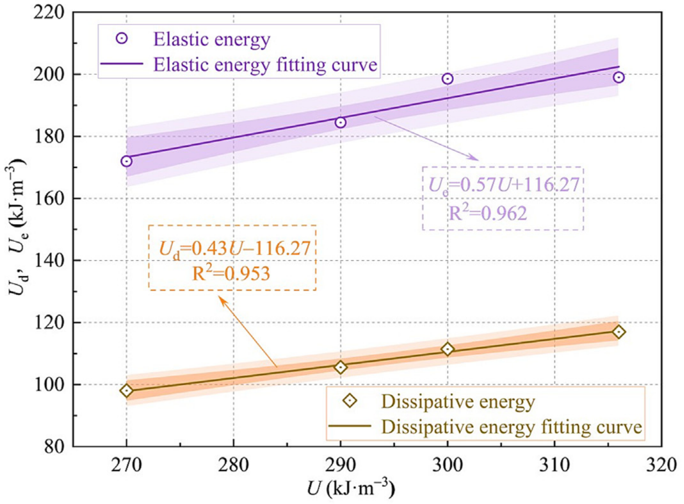

(c) Joint failure

Fig. 22. Fitting curves of the linear energy storage law for specimens under different failure modes.

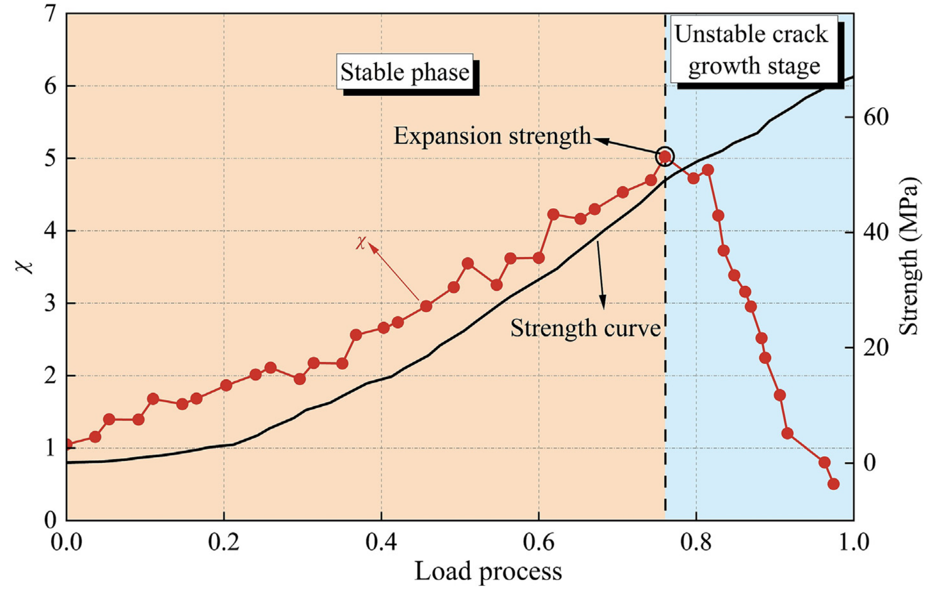

Fig. 23. Variation of characteristic energy during the loading process.

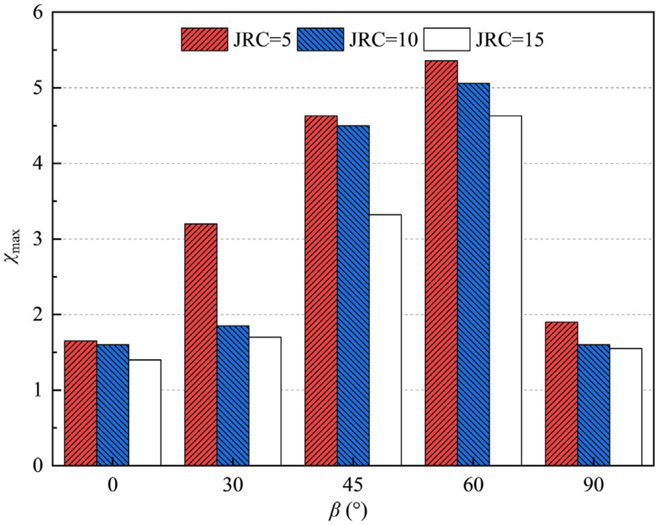

Fig. 24. $\chi_{\max}$ under different JRC.

4.2.2. Validation of mesoscopic parameters reasonableness

To ensure that the macroscopic mechanical behavior of the numerical simulation specimens accurately reflects the physical laboratory test results, this section selects specimens with a JRC of 10 and joint dip angles of 0°, 45°, and 90° for comparison between the simulation results and laboratory tests. The specific comparison is shown in Fig. 26.

The figure shows that there are certain differences between the stress-strain curves obtained from laboratory tests and those obtained from numerical simulations. The laboratory specimens experienced typical stages, including compaction, elastic deformation, yielding, and failure, whereas the numerical simulation specimens directly entered the elastic deformation stage after loading. This is because during the generation of the PFC2D model, the voids between particles are compacted by pre-consolidation force, resulting in the absence of a distinct compaction stage in the simulation curves. Ignoring the compaction stage, the simulated and experimental stress-strain curves show good overall agreement, with small differences in peak strength and elastic modulus.

Table 7
Mesoscopic parameters.

Mesoscopic	Material type		
	Material A	Material B	Joint
Minimum particle radius, $r_{\min}$ (mm)	0.1	0.1	0.3
Particle size ratio, $r_{\min}$ / $r_{\max}$	3	3	3
Particle density, ρ (kg/m^3)	1	1	1
Particle contact modulus, E_c (GPa)	18	14.2	5.4
Particle stiffness ratio, k_n/k_s	0.5	0.5	0.15
Friction coefficient, μ	0.5	0.5	0.15
Contact modulus, $\bar{E}$ (GPa)	14	13	4.2
Contact stiffness ratio, $\bar{k}_n$ / $\bar{k}_s$	1	1	1
Parallel bond factor	1	1	0.5
Phase strength by parallel bonding method, pb_s_n (MPa)	26	20	7.8
Tangential strength of parallel bond, pb_s_s (MPa)	20	16	6

Moreover, under different joint dip angles, the failure modes obtained from numerical simulations are highly consistent with those observed in laboratory tests, effectively reproducing the failure characteristics of the specimens. Therefore, the rock model established in this study and the calibrated mesoscopic parameters are highly rational and accurate, validating the reliability of the laboratory test results.

4.3. Analysis of the numerical simulation results

To clarify the crack evolution process during loading, Fig. 27 shows the model's stress-strain curves with marked characteristic points. Corresponding microcrack distribution maps at each characteristic point are also presented for intuitive observation of crack propagation.

Fig. 27a shows the stress-strain curve and microcrack evolution process of the model with a joint dip angle of 0°. At the initial loading stage, tensile microcracks initiate first along the joint and gradually propagate into the matrix regions on both sides. The microcrack density within the weak matrix is significantly higher than that in the strong matrix, indicating pronounced asymmetry. The strength difference between the two matrix sides substantially influences the initiation and propagation behavior of microcracks. As loading continues, the number of microcracks increases gradually, shear microcracks start to emerge, and their quantity rapidly increases near the peak strength. Ultimately, shear microcracks

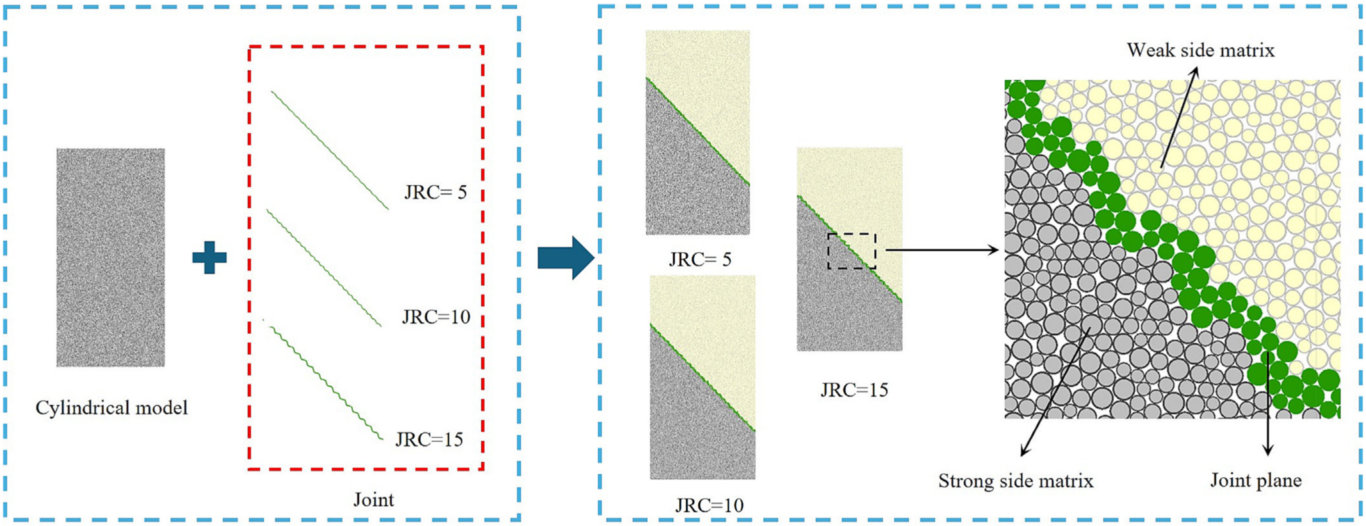

Fig. 25. Schematic diagram of numerical simulation model establishment.

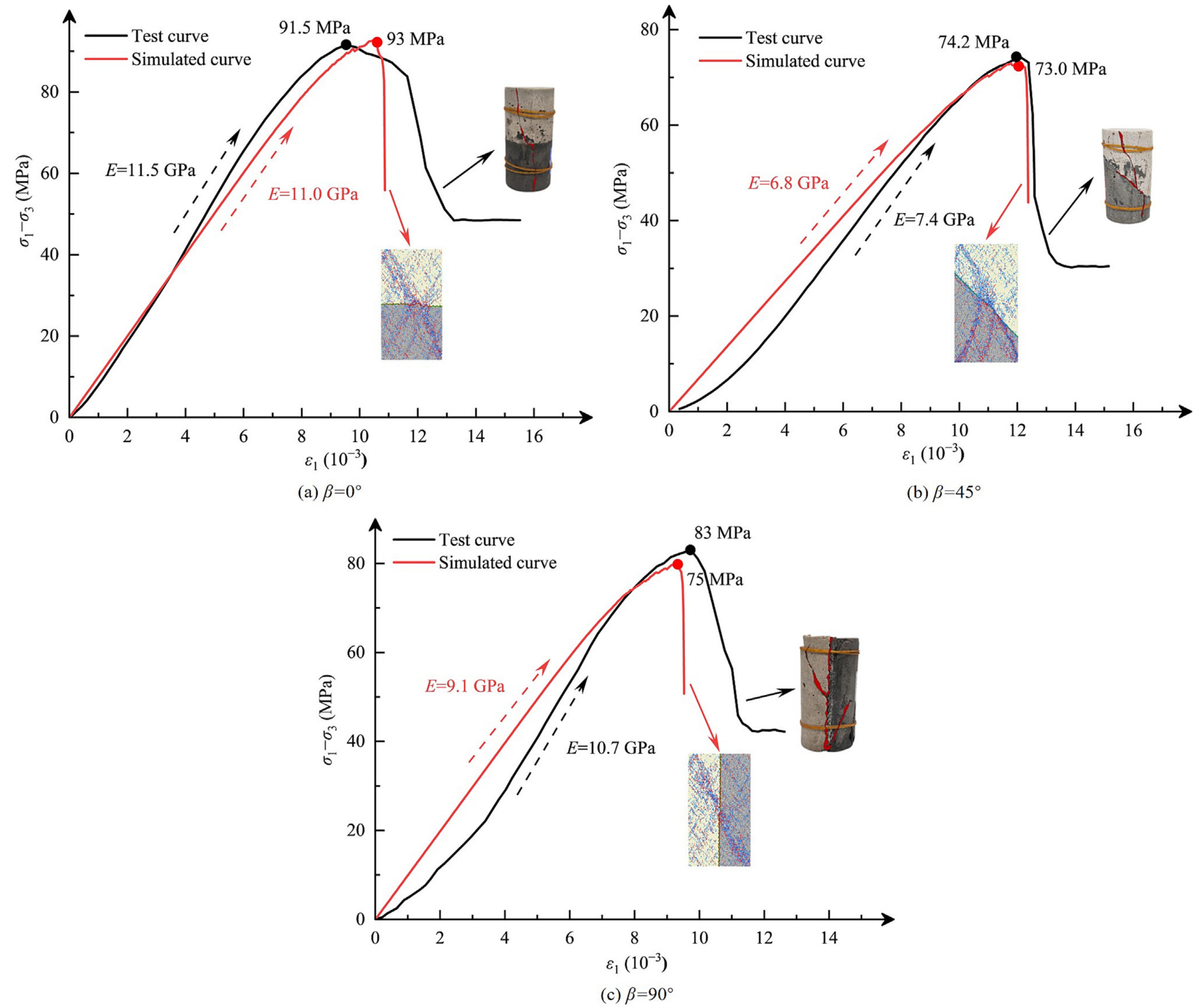

(a) β=0°

(b) β=45°

(c) β=90°

Fig. 26. Comparison of the mechanical curves and failure modes between the numerical simulations and laboratory tests.

become dominant, forming an inclined shear failure band that traverses the joint plane in the model.

Fig. 27b displays the stress-strain curve and crack evolution process for the model with a joint dip angle of 45°. At the initial loading stage, cracks are mainly concentrated around the joint surface, primarily as shear cracks with a relatively uniform distribution. In this early stage, the joint surface guides crack initiation, with crack propagation directions coinciding with the joint plane, indicating shear-dominated failure. As loading progresses, the number of shear cracks increases gradually, especially near the peak strength. Significant sliding failure occurs along the joint surface, and shear cracks extend along the joint into the matrix, eventually forming a shear failure band penetrating through the joint.

When the joint dip angle is 90° (Fig. 27c), tensile cracks initiate from the joint region during the early loading stage. However, since the joint surface is parallel to the loading direction, stress transfer is ineffective, significantly limiting crack propagation and preventing further development. Subsequently, numerous cracks initiate within the matrix, with the crack density on the weaker matrix side noticeably higher than that on the stronger side, indicating asymmetric damage characteristics between the strong and weak matrices. As loading approaches the peak strength, shear cracks emerge in large quantities and gradually dominate. In the late loading stage, shear cracks form a through-going shear failure band on the weaker matrix side. In contrast, the crack distribution on the stronger matrix side remains sparse without forming a continuous failure band. The crack evolution process indicates that although microcracks initiate first in the joint area, the shear crack band formed in the matrix is the main cause of model failure.

4.4. Microscopic damage analysis

(1) Microcrack distribution

The spatial distribution of microcracks can be classified into four types: joint shear cracks, joint tensile cracks, matrix shear cracks, and matrix tensile cracks. Fig. 28 shows the distribution of microcracks inside the matrix and joints of the composite joint model with a JRC of 10.

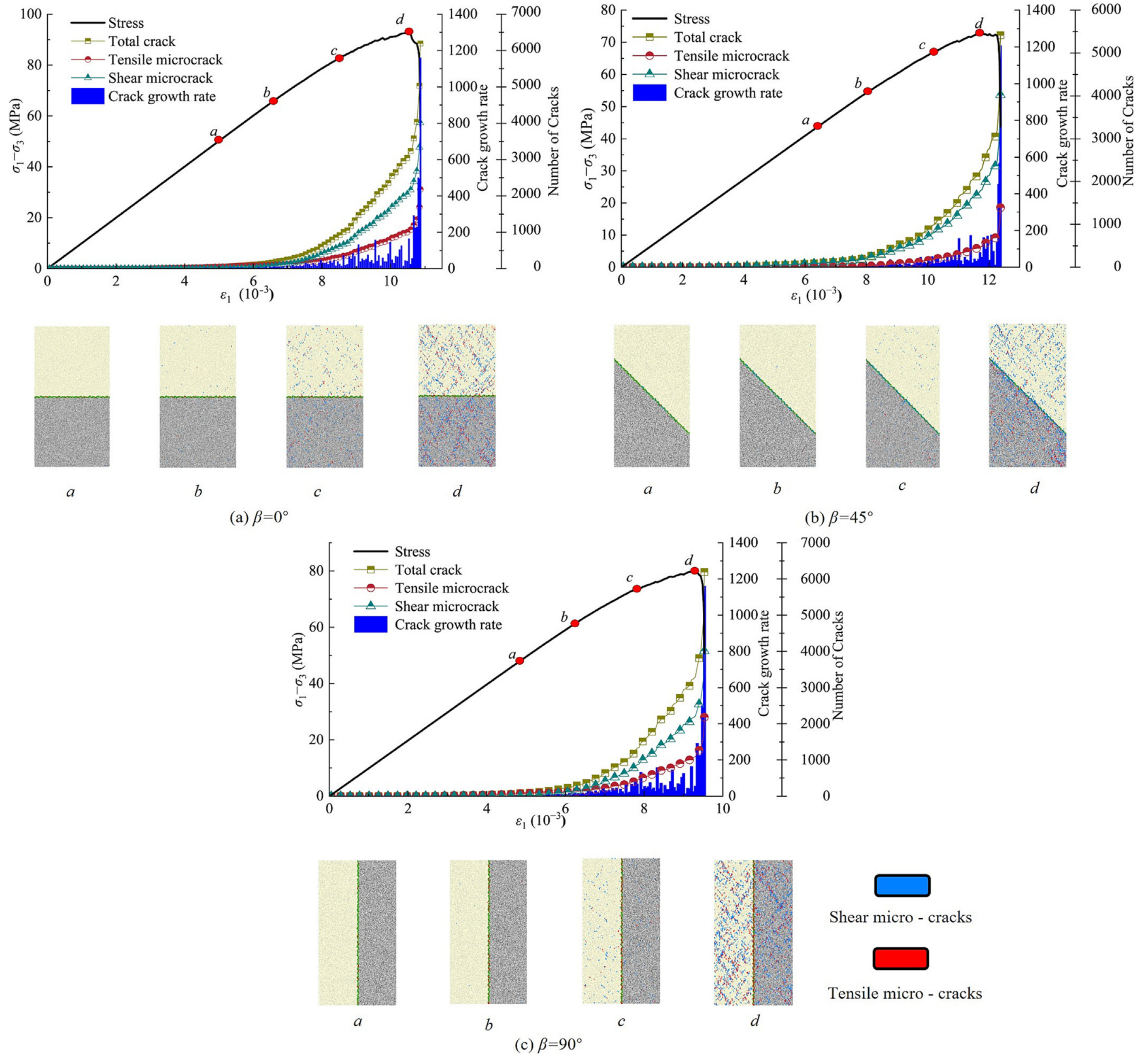

(a) β=0°

(b) β=45°

(c) β=90°

Fig. 27. Microscopic evolution process of the joint model.

In terms of joint crack distribution characteristics, the proportion of joint tensile cracks first decreases and then increases as the joint dip angle increases, whereas the proportion of joint shear cracks first increases but then decreasing. Regarding matrix crack distribution, the proportion of matrix tensile cracks continuously increases with increasing joint dip angle, whereas the proportion of matrix shear cracks continuously decreases.

This reveals the regulatory effect of the joint dip angle on the crack evolution mechanism inside the jointed rock mass. Under low dip angles (0°–30°), damage within the matrix is dominated by shear cracks controlled by shear stress, whereas the joint surfaces mainly develop tensile cracks due to tensile stress. When the joint dip angle ranges from 45° to 60°, the matrix cracks transition gradually from shear-dominated to tension-dominated, and the proportion of shear cracks inside the joints significantly increases, shifting the failure mode from tension-controlled to shear-controlled. At a dip angle of 90°, the proportions of tensile cracks in both the matrix and the joint surface increase markedly, dominating the matrix failure and enhancing the tensile stress effect.

Figs. 29a and b illustrate the influence of joint roughness on the proportion of microcrack types inside the matrix and the joint, respectively. The proportion of shear cracks inside both the matrix and the joint gradually increases with increasing joint roughness, which suppresses the initiation of tensile cracks. For the matrix, this is because the rough joint surface enhances the interaction between the matrix and the joint, increasing the resistance of the joint surface against shear, thereby promoting the formation of shear cracks. This trend indicates that increasing joint roughness strengthens the coupling effect between the joint surface and the matrix, making the shear failure characteristics in the matrix more pronounced. For the joint itself, the higher roughness enhances the

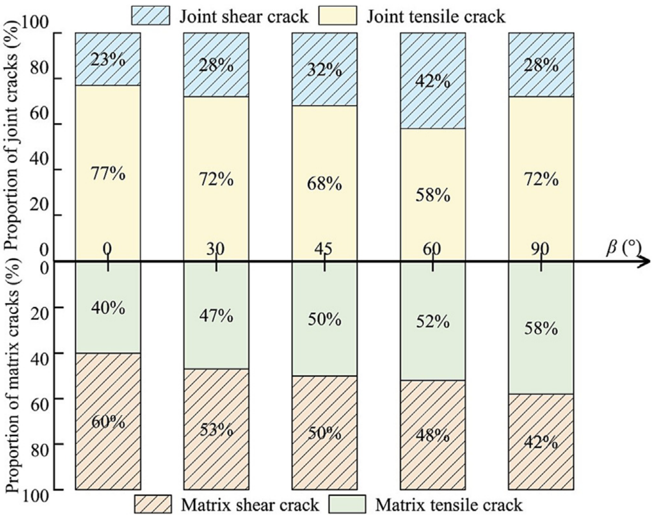

Fig. 28. Evolution trends of the proportions of microcrack types inside the matrix and joints with joint dip angle (JRC = 10, σ_3=8 MPa).

interlocking effect, allowing shear stress to accumulate more easily along the joint surface, which promotes shear failure.

(2) Local damage coefficient.

To investigate the influence of the joint roughness and joint dip angle on the mesoscopic damage characteristics of the specimen, the damage coefficients *Z* of the matrix and joint under different conditions were calculated via Eq. (18):

$$Z = \frac{M}{C} \times 100\% \tag{18}$$

where *M* represents the number of microcracks within the matrix or joint region; and *C* the total number of contacts in the matrix or joint region.

Fig. 30 illustrates the variation of the matrix damage coefficient and joint damage coefficient with joint dip angle when the JRC is 10. As shown in the figure, the matrix and joint damage coefficients exhibit opposite trends as the joint dip angle increases. The matrix damage coefficient first decreases and then increases with increasing joint dip angle, indicating that the degree of matrix damage initially decreases and subsequently intensifies. Conversely, the joint damage coefficient initially increases but then decreases with increasing joint dip angle. The increase in joint roughness enhances the shear resistance of the joint surface, thereby strengthening the constraint on crack propagation and, to some extent, reducing the joint damage coefficient. However, higher roughness can also lead to stress concentrations at contact interfaces, potentially resulting in higher microcrack density in localized regions, which increases the matrix damage coefficient.

5. Discussion

Previous studies have predominantly focused on jointed rock masses composed of homogeneous materials, and numerous mechanical experiments have been conducted to examine the influence of joint dip angle and joint roughness on failure modes. However, these studies have largely neglected the complex coupling mechanisms arising from the strength heterogeneity between the materials on either side of the joint—particularly in cases where the weaker matrix does not exhibit markedly low strength.

In this study, anisotropic composite specimens with differing matrix strengths and regularly serrated joints were designed to systematically investigate the influence of joint geometry on failure mode evolution, energy response, and microcrack damage mechanisms under triaxial stress conditions. Based on experimental results, the PFC2D discrete element method was introduced to simulate the evolution of microcracks, thereby establishing an integrated research framework that links macroscopic responses to microscopic mechanisms. Compared with existing studies, this work offers significant advantages in revealing the transition of failure modes, the evolution of dominant crack types, and energy dissipation mechanisms under the coupled control of joints and matrix materials.

Despite these meaningful findings, several limitations should be acknowledged:

(1) Material simulation: Cement mortar was used to simulate natural rock. Although it ensured consistency in specimen preparation and parameter control, it differs from natural rock in terms of long-term loading behavior, water saturation, and chemical erosion resistance.

(2) Single confining pressure: The triaxial tests were conducted under a constant confining pressure of 8 MPa, without considering the influence of varying burial depths or in-situ

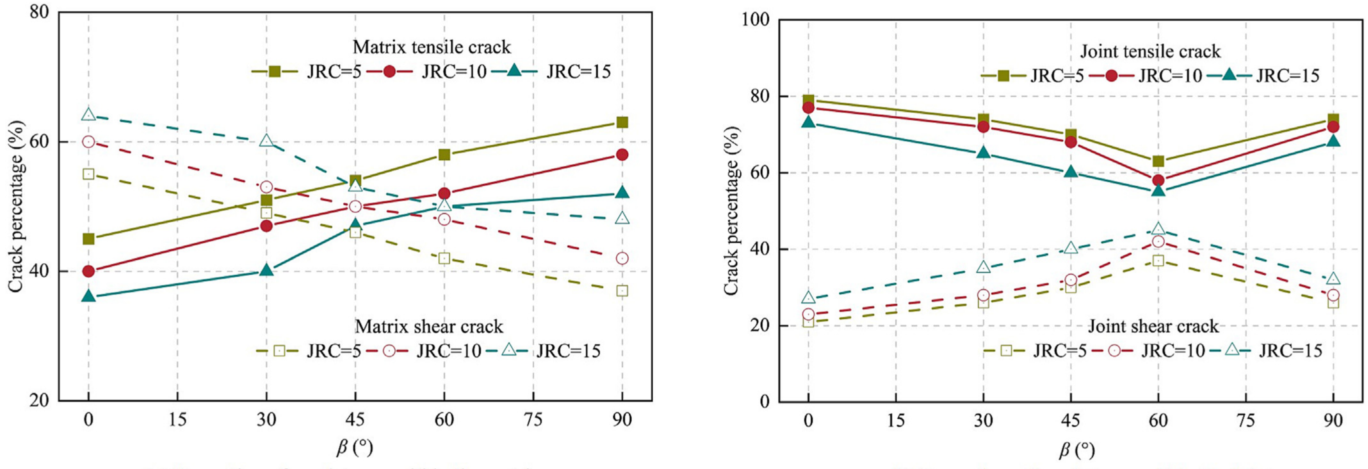

(a) Proportion of crack types within the matrix

(b) Proportion of crack types within the joint

Fig. 29. Variation trends in the proportions of crack types within the matrix and joint under different joint roughness conditions.

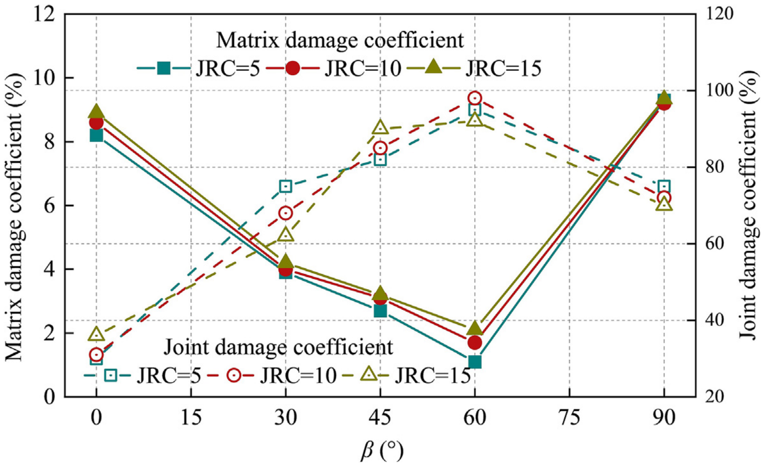

Fig. 30. Variation of damage coefficients with joint dip angle.

stress states. Future studies should expand the range of confining pressures to increase the generalizability of the results.

(3) Simplified joint modeling: Both the 3D-printed molds used in physical testing and the idealized serrated joint model used in numerical simulations oversimplify the irregular morphology and multiscale roughness of natural joints.
(4) Limited damage indicators: This study primarily focuses on mesoscopic damage analysis based on statistical evaluations of crack quantity and type, and does not yet incorporate multi-physical field coupling factors such as acoustic emission, stress redistribution, and seepage evolution.

These limitations may affect the direct applicability of the results to field-scale engineering problems. Nevertheless, within the controlled parameter range of this study, the key trends observed demonstrate strong generality and provide valuable insights. Future research should consider incorporating more complex joint geometries, multiscale matrix heterogeneity, and environmental coupling factors to enhance the engineering relevance and predictive capability of the proposed model.

6. Conclusions

(1) Three typical failure modes were observed in the specimens: joint failure, mixed failure, and matrix shear failure. The joint dip angle is the dominant factor controlling the failure mode, whereas the joint roughness plays a regulatory role. The joint dip angle influences the stress state along the joint plane, thereby affecting the overall failure behavior of the specimen. A clear correlation was found between the failure mode and the peak strength of the specimen: when the failure mode transitions from joint failure to mixed failure and then to matrix shear failure, the corresponding peak strength decreases accordingly.
(2) The mechanical parameters of the specimens exhibit pronounced anisotropy. Increasing the joint roughness not only significantly reduces the degree of anisotropy but also enhances the crack initiation stress and dilatancy stress. This results in a reduced proportion of the post-peak unstable development phase, thereby reducing the brittleness of the specimen.
(3) A greater joint roughness markedly improves the energy storage capacity of the specimen and prolongs the failure process. The peak elastic energy is strongly influenced by the joint dip angle, with the lowest peak elastic energy observed at a dip angle of 60°. A clear linear relationship exists between the elastic energy and the peak deviatoric stress, validating the applicability of the linear energy storage law.
(4) The discrete element results indicate that the joint dip angle significantly influences the initiation, propagation, and accumulation of microcracks, as well as the overall failure mode. With increasing joint dip angle, the concentration zone of microcracks shifts from the matrix to the joint, and the dominant microcrack type transitions from tensile to shear and then back to tensile cracks. In contrast, increasing the joint roughness reduces damage along the joint and notably weakens the influence of the joint on the spatial location of the specimen's failure surface.

Acknowledgements

This research was supported by the National Natural Science Foundation of China (Nos. 52304108, 52274148), and China University of Mining and Technology-Beijing Undergraduate Innovation Training Program (No. 202515011).

References

[1] Deng HW, Liu CJ, Ke B, Wang Y, Zhang YN. Experimental study on microscopic damage characteristics of granite under cyclic dynamic disturbances. Chin J Eng 2017;39(11):1634–9. In Chinese.
[2] Qian QH. Challenges faced by underground projects construction safety and countermeasures. Chin J Rock Mech Eng 2012;31(10):1945–56. In Chinese.
[3] Liu XR, Kou MM, Lu YM, Liu YQ. An experimental investigation on the shear mechanism of fatigue damage in rock joints under pre-peak cyclic loading condition. Int J Fatigue 2018;106:175–84.
[4] Brace WF, Kohlstedt DL. Limits on lithospheric stress imposed by laboratory experiments. J Geophys Res Solid Earth 1980;85(B11):6248–52.
[5] Zheng Z, Deng B, Liu H, Wang W, Huang S, Li S. Microdynamic mechanical properties and fracture evolution mechanism of monzogabbro with a true triaxial multilevel disturbance method. Int J Min Sci Technol 2024;34(3):385–411.
[6] Wang ZC, Shi WC, Kong R, Guo JF. Mechanical properties of deep sandstone under true triaxial stress. J Northeast Univ Nat Sci 2023;44(5):689–96. In Chinese.
[7] Shan RL, Liu NZ, Sun P, Zhao ZY, Dong RY, Dou HY, Bai Y. Experimental and numerical simulation study of rough jointed rock samples under triaxial compression conditions. Eng Fract Mech 2025;314:110707.
[8] He M, Peng Y, Zhao S, Shi H, Wang N, Gong W. Fracture mechanism of inversed trapezoidal shaped tunnel excavated in 45 inclined rock strata. Int J Min Sci Technol 2015;25(4):531–5.
[9] Abbas N, Li KG, Fissha Y, Khatti J, Geberegergis MB, Cheepurupalli NR, Chandrahas NS. Reliability analysis of support strategies in tunnel

construction: Insights from geomechanical analysis of jointed rock masses. Results Earth Sci 2024;2:100044.

[10] Zhang H, Lu CP, Liu B, Liu Y, Zhang N, Wang HY. Numerical investigation on crack development and energy evolution of stressed coal-rock combination. Int J Rock Mech Min Sci 2020;133:104417.

[11] Liu XG, Zhu WC, Zhang PH, Li LK. Failure in rock with intersecting rough joints under uniaxial compression. Int J Rock Mech Min Sci 2021;146:104832.

[12] Asadizadeh M, Hossaini MF, Moosavi M, Masoumi H, Ranjith PG. Mechanical characterisation of jointed rock-like material with non-persistent rough joints subjected to uniaxial compression. Eng Geol 2019;260:105224.

[13] Huang SB, Liu QS, Liu YZ, Kang YS, Cheng AP, Ye ZY. Frost heaving and frost cracking of elliptical cavities (fractures) in low-permeability rock. Eng Geol 2018;234:1–10.

[14] Yan YT, Wang SW. Simulation investigation of mechanical and failure characteristics of jointed rock with different shapes of joint asperities under compression loading. Computational Particle Mechanics 2023;10(1):45–59.

[15] Yuan P, Li AB, Chen CN, Lu XF. Experimental study of uniaxial compressive mechanical properties of rough jointed rock masses based on 3D printing. Appl Rheol 2023;33:20230114.

[16] Peellage WH, Fatahi B, Rasekh H. Experimental investigation for vibration characteristics of jointed rocks using cyclic triaxial tests. Soil Dyn Earthq Eng 2022;160:107377.

[17] Chen QZ, Liu YM, Pu SY. Strength characteristics of nonpenetrating joint rock mass under different shear conditions. Adv Civ Eng 2020;2020(1):3579725.

[18] Yin DW, Chen SJ, Ge Y, Liu R. Mechanical properties of rock–coal bi-material samples with different lithologies under uniaxial loading. J Mater Res Technol 2021;10:322–38.

[19] Liu XB, He SH, Wang DH. Numerical analysis of the anisotropy and scale effects on the strength characteristics of defected rockmass. Adv Civ Eng 2020;2020 (1):5892924.

[20] Ma Q, Tan YL, Liu XS, Zhao ZH, Fan DY. Mechanical and energy characteristics of coal–rock composite sample with different height ratios: a numerical study based on particle flow code. Environ Earth Sci 2021;80(8):309.

[21] He YC, Zhao PX, Li SG, Ho CH, Zhu ST, Kong XG, Barbieri DM. Mechanical properties and energy dissipation characteristics of coal–rock-like composite materials subjected to different rock–coal strength ratios. Nat Resour Res 2021;30(3):2179–93.

[22] Liu XW, Liu QS, Kang YS, Pan YC. Improved nonlinear strength criterion for jointed rock masses subject to complex stress states. Int J Geomech 2018;18 (3):04017164.

[23] Han Y, Zhao YM, Li JL. Experimental and numerical study of strength and failure behavior of precracked marble under true triaxial compression. Shock Vib 2021;2021(1):3869045.

[24] Chi XL, Yang K, Wei Z. Investigation of energy and damage evolutions in rock specimens with large-scale inclined prefabricated cracks by uniaxial compression test and AE monitoring. Adv Civ Eng 2020;2020(1):8887543.

[25] Wang YY, Yang HQ, Song KL, Chen CW, Li H, Li XY. The influence of joint distribution characteristics on the mechanical properties, fracture mechanisms, and energy characteristics of rock masses under stress conditions. Comput Geotech 2025;178:106933.

[26] Zhang HQ, Shi H, Zhao HY, Song L. Characterization of transverse vibration response of resin-anchored bolt under axial tension and life cycle health assessment of anchorage debonding. Measurement 2025;256:118273.

[27] Yin PF, Yang SQ. Experimental study on strength and failure behavior of transversely isotropic rock-like material under uniaxial compression. Geomech Geophys Geo Energy Geo Resour 2020;6(3):44.

[28] Meng YY, Jing HW, Zhou ZF, Zhang L, Sun SH. Experimental investigation on the mixed-mode fracture behavior of rock-like material with bedding plane. Theor Appl Fract Mech 2022;117:103159.

[29] Liu HB, Cui S, Meng YF, Sun HR, Wang S, Du S. Study on the mechanical properties and failure law of rocks with interbedded sand and mud. ACS Omega 2022;7(49):44804–16.

[30] Dou HY, Shan RL, Li GZ, Sun P, Bai Y, Qiu SH. Research on the Brazilian splitting characteristics and failure mechanism of jointed composite disks. mech Adv. Mater Struct 2025;32(12):2762–77.

[31] Xie HP. Fractal description of rock joints. Chin J Geotech Eng 1995;17(1):18–23. In Chinese.

[32] Kong LY, Ishutov S, Hasiuk F, Xu CC. 3D printing for experiments in petrophysics, rock physics, and rock mechanics: a review. SPE Reserv Eval Eng 2021;24(4):721–32.

[33] Gell EM, Walley SM, Braithwaite CH. Review of the validity of the use of artificial specimens for characterizing the mechanical properties of rocks. Rock Mech Rock Eng 2019;52(9):2949–61.

[34] Bai Y, Shan RL, Wu YX, Sun PF. Development and application of a new triaxial testing system for subzero rocks. Geotech Test J 2021;44(5):1327–49.

[35] Shi XD, Feng GR, Bai JW, Zhu C, Wang SY, Wang K, Song C. Brazil splitting characteristics of coal-backfilling composite structure with different interface angles: Insights from laboratory experiment and numerical simulation. J Cent South Univ 2023;30(1):189–201.

[36] Meng YY, Jing HW, Sun SH, Chen M, Huang K. Experimental and numerical studies on the anisotropic mechanical characteristics of rock-like material with bedding planes and voids. Rock Mech Rock Eng 2022;55(11):7171–89.

[37] Zhang ZH, Liang ZZ, Tang CA, Kishida K. A comparative study of current methods for determining stress thresholds of rock subjected to compression. Rock Mech Rock Eng 2023;56(11):7795–818.

[38] Gao L, Gao F, Zhang ZZ, Xing Y. Research on the energy evolution characteristics and the failure intensity of rocks. Int J Min Sci Technol 2020;30(5):705–13.

[39] Zhang JW, Song ZX, Wang SY. Experimental investigation on permeability and energy evolution characteristics of deep sandstone along a three-stage loading path. Bull Eng Geol Environ 2021;80(2):1571–84.

[40] Hou ZK, Gutierrez M, Ma SQ, Almrabat A, Yang CH. Mechanical behavior of shale at different strain rates. Rock Mech Rock Eng 2019;52(10):3531–44.

[41] Gong FQ, Zhang PL, Luo S, Li JC, Huang D. Theoretical damage characterisation and damage evolution process of intact rocks based on linear energy dissipation law under uniaxial compression. Int J Rock Mech Min Sci 2021;146:104858.

[42] Xu L, Gong FQ, Luo S. Effects of pre-existing single crack angle on mechanical behaviors and energy storage characteristics of red sandstone under uniaxial compression. Theor Appl Fract Mech 2021;113:102933.